UPPSALA
UNIVERSITET

Digital Comprehensive Summaries of Uppsala Dissertations from the Faculty of Science and Technology 874

X-ray Spectroscopic Studies of Materials for Nuclear Technology

JOHAN VEGELIUS

ACTA
UNIVERSITATIS
UPSALIENSIS
UPPSALA
2011

ISSN 1651-6214
ISBN 978-91-554-8205-3
urn:nbn:se:uu:diva-160362

Dissertation presented at Uppsala University to be publicly examined in Polhemsalen, Ångströmlaboratoriet, Lägerhyddsvägen 1, Uppsala. Friday, December 9, 2011 at 10:15 for the degree of Doctor of Philosophy. The examination will be conducted in English.

Abstract
Vegelius, J. 2011. X-ray Spectroscopic Studies of Materials for Nuclear Technology. Acta Universitatis Upsaliensis. *Digital Comprehensive Summaries of Uppsala Dissertations from the Faculty of Science and Technology* 874. 56 pp. Uppsala. ISBN 978-91-554-8205-3.

X-ray spectroscopic experiments, including X-ray absorption spectroscopy (XAS), X-ray emission spectroscopy (XES) and resonant inelastic X-ray scattering (RIXS), were performed in a large energy range (60-9000 eV) on a variety of systems, probing different elements and orbitals. The systems can preferably be divided into three groups: Actinides, copper systems and amorphous materials. We studied oxidation states of Pu in PuO_2 using a closed-source experimental setup, developed by us, to lower the safety restrictions associated with such experiments. The presence of Pu with higher oxidation state than Pu(IV) was found in polycrystalline PuO_2. This is an important finding since Pu with higher oxidation states has higher solubility affecting the safety of a proposed undeground repository of spent nuclear fuel which can eventually be infiltrated by groundwater. In the proposed underground repository the molecular oxygen will vanish at some point due to microbial activity and mineral oxidation. At this stage sulfur is the most important candidate for causing copper corrosion. We studied Cu films and foils exposed to sulfide solutions at both Cu $L_{2,3}$, Cu K and S $L_{2,3}$ edges and found for example that S $L_{2,3}$ XES is useful for distinguishing between different copper sulfides and Cu Kβ XES can be used to identify monovalent Cu compounds. Amorphous, zirconium containing alloys are potentially useful materials for future nuclear reactors. The electronic structure of such materials was also investigated.

Keywords: XAS, XES, RIXS, amorphous, DOS, spectroscopy, actinides, copper, uranium, plutonium

Johan Vegelius, Uppsala University, Department of Physics and Astronomy, Soft X-Ray Physics, 516, SE-751 20 Uppsala, Sweden.

ISSN 1651-6214
ISBN 978-91-554-8205-3
urn:nbn:se:uu:diva-160362 (http://urn.kb.se/resolve?urn=urn:nbn:se:uu:diva-160362)

To friends and family

List of Papers

This thesis is based on the following papers, which are referred to in the text by their Roman numerals.

I **U 5d RIXS on uranium compounds**
J. Vegelius, A. Modin, D. K. Shuh and S. M. Butorin
In manuscript

II **Closed source experimental system for soft x-ray spectroscopy of radioactive materials**
A. Modin, S. M. Butorin, J. Vegelius, A. Olsson, C.-J. Englund, J. Andersson, L. Werme, J. Nordgren, T Käämbre, G. Skarnemark and B. E. Burakov
Review of scientific instruments, vol. 79, n. 9, p. 093103 (2008)

III **Indication of single-crystal PuO_2 oxidation from O 1*s* x-ray absorption spectra**
A. Modin, Y. Yun, M.-T. Suzuki, J. Vegelius, L. Werme, J. Nordgren, P. M. Oppeneer and S. M. Butorin
Physical Review B, vol. 83, 075113 (2011)

IV **Electron transfer during selenium reduction by iron surfaces in aqueous solution: high resolution X-ray absorption study**
K. O. Kvashnina, S. M. Butorin, D. Cui, J. Vegelius, A. Puranen, R. Gens and P. Glatzel
Journal of Physics: Conference Series, vol. 190, p. 012191 (2009)

V **X-ray spectroscopic study of Cu_2S, CuS and copper films exposed to Na_2S solutions**
J. Vegelius, K. O. Kvashnina, H. Hollmark, M. Klintenberg, Y. Kvashnin, I. L. Soroka, L. Werme and S. M. Butorin
submitted to Phys. Rev. B

VI **Exposure of oxidized copper surfaces to aqueous Na_2S solution studied with soft X-ray spectroscopy**
H. M. Hollmark, J. Vegelius, P. Kristiansen, L. Werme and L.-C. Duda,

Journal of the Electrochemical Society, vol. 158, C1 (2011)

VII **Cu K$\beta_{2,5}$ X-ray emission spectroscopy as a tool for characterization of monovalent copper compounds**
J. Vegelius, K. O. Kvashnina, M. Klintenberg, I. L. Soroka and S. M. Butorin
In manuscript

VIII **Structural stability and oxidation resistance of amorphous Al-Zr alloys**
I.L. Soroka, J. Vegelius, P.T. Korelis, A. Fallberg, S. M. Butorin and B. Hjörvarsson
Jornal of Nuclear Materials, vol. 401, 38 (2010)

IX **Atomic and electronic structure of amorphous Al-Zr alloys**
J. Vegelius, I. Soroka, P. T. Korelis, B. Hjörvarsson and S. M. Butorin
Journal of Physics: Condensed Matter vol. 23, 265503 (2011)

X **Temperature dependence of electrical resistivity of amorphous Fe-Zr films and multilayers**
J. Vegelius, G. K. Pálsson, P. T. Korelis, M. Haverhals, S. M. Butorin, A. Modin, M. Kavčič, M. Žitnik K. Bučar, K. O. Kvashnina, V. Kapaklis and B. Hjörvarsson
submitted to Phys. Rev. B

Reprints were made with permission from the publishers.

Contents

1 Sammanfattning på svenska 9
2 Introduction 11
2.1 Ψ 11
3 Nuclear related materials 13
3.1 Actinides 13
3.2 Copper as material for spent fuel canister 13
3.3 Amorphous zircaloys 14
4 Theoretical base for spectroscopy 17
4.1 Atomic theory 17
4.2 Solid state theory 18
4.3 Transition matrix element 21
4.3.1 Dipole approximation 21
5 X-ray spectroscopic techniques 23
5.1 X-ray absorption spectroscopy 23
5.2 X-ray emission spectroscopy 24
5.3 Resonant inelastic X-ray scattering 27
5.4 X-ray absorption spectroscopy in the high energy resolution fluorescence detection mode 29
5.5 Spectrometers 30
5.5.1 Grazing-incidence spectrometer for soft X-rays 31
5.5.2 Crystal analyzer spectrometer for hard X-rays 32
6 Results 33
6.1 PuO_2 oxidation 33
6.2 Se(IV) reduction 36
6.3 Copper corrosion 38
6.3.1 Copper sulfidation 38
6.3.2 Monovalent copper compounds 41
6.4 Thermal treatment of amorphous alloys 46
6.4.1 Al-Zr 46
6.4.2 Fe-Zr 48
7 Acknowledgements 53
Bibliography 55

1. Sammanfattning på svenska

I det här arbetet studeras övergångar mellan elektroniska tillstånd i olika material. Ett elektroniskt tillstånd svarar mot en så kallad elektronisk vågfunktion som enligt kvantmekaniken bär på all fysikalisk information om tillståndet i fråga. För en isolerad väteatom kan dessa tillstånd beräknas exakt och kallas Ψ_{nl} där n (1,2,3,...) är huvudkvanttalet och l (0,1,2,..,$n-1$) är rörelsemängdsmomentskvanttalet. Varje tillstånd kan förknippas med ett energiegenvärde E_{nl} som svarar mot systemets energi. Systemet kan endast ha dessa energier och inga däremellan. Tillstånden i väteatomen kallas orbitaler, till exempel 1s, 2p, etc. I större atomer, molekyler och material används ofta fortfarande dessa tillstånd som baser så terminologin från väteatomen kan således behållas.

I röntgenspektroskopier (X-ray spectroscopies) används synkrotronljus för att excitera hårt bundna elektroner till lediga tillstånd i valensbandet eller till kontinuumet ovanför jonisationsenergin. Då bildas ett ledigt tillstånd[1] djupt i atomen i vilket den hård bundna elektronen förut satt. En elektron i ett tillstånd med högre energi kommer inom mycket kort tid att avge energi och inta den tidigare hårt bundna elektronens plats djupt inne i atomen. Systemet avger då energi antingen i form av en elektron i valensbandet (troligast) eller i form av en foton (minst troligt). Fotonens energi svarar mot skillnaden i energi mellan de två tillstånden som är inblandade i övergången och det är dessa fotoner vi är intresserade av inom röntgenspektroskopi. Den djupt liggande energinivån, till exempel 1s, fungerar som referenspunkt och är ämnesspecifik vilket gör att röntgenspektroskopi är ämnesspecifikt.

Generellt kan man säga att två röntgenspektroskopier använts. I den ena varieras energin hos det inkommande ljuset kontinuerligt och graden av absorption i materialet mäts som funktion av inkommande energi. På så sätt mäts mängden lediga tillstånd i ett material vid olika energier. Detta kallas XAS (X-ray absorption spectroscopy). I den andra metoden används bara en energi för inkommande ljus och det ljus som emitteras mäts energiupplöst. På så sätt fås ett mått på mängden ockuperade tillstånd i materialet. Detta kallas XES (X-ray emission spectroscopy). I båda metoderna används referensnivån hos den exciterade elektronen som tidigare var starkt bunden till atomen, till exempel en 1s-elektron. Vid de energier vi använder för det inkommande ljuset gäller den så kallade dipolapproximationen. Det betyder bland annat att i princip bara

[1] Pauliprincipen säger att det endast får finnas en elektron med exakt samma uppsättning kvanttal. På så sätt bildas ett "ledigt" tillstånd när en elektron försvinner från sitt tillstånd.

övergångar som ändrar l-kvanttalet med 1 förekommer. Detta betyder i sin tur att vi inte studerar alla tillstånd i valens- och ledningstillstånd utan orbitaler studeras selektivt. Röntgenspektroskopier är således inte bara ämnesspecifika utan även orbitalspecifika.

Experiment med olika material och vid olika synkrotroner har genomförts i ett stort energiintervall ($\sim$70-9000 eV). På så sätt har många olika element och orbitaler studerats selektivt.

I detta arbete har dessa tekniker tillämpats på material relevanta för kärnteknik. Det experimentella arbetet har utförts vid synkrotronanläggningar med inställbar energy hos inkommande fotoner. Vi utvecklade en inneslutningsmetod som kan användas vid studier av aktinider och andra ämnen som är associerade med strikta säkerhetsbestämmelser vid hantering, arbete och transport till experimentella anläggningar. Experimentet bidrog till kunskap om oxidationstillstånd hos Pu.

Vi har undersökt kopparföreningar. Vi visade bland annat att Cu K$\beta_{2,5}$ röntgenemission-spektroskopi (p-tillstånd i valensbandet hos Cu fyller det nyligen bildade elektronhålet i Cu 1s-orbitalen) kan användas för att skilja mellan olika kopparföreningar med oxidationstillstånd Cu(I). En pågående debatt gäller tesen att Cu alltid befinner sig i oxdationstillståndet Cu(I) i kopparsulfidföreningar. Vi har funnit tecken på Cu med högre valenstal än Cu(I) i CuS med hjälp av en medod att mäta röntgenabsorptionsspektroskopi genom att selektivt mäta utgående fotoner med en specifik energi och på så sätt minska livstidsbreddningen av det kortlivade exciterade tillståndet. På så sätt förbättrades upplösningen signifikant och gjorde tolkningen otvetydig.

Elektronstrukturen hos amorfa material såsom Fe-Zr- och Al-Zr-legerinar har undersökts. Fe-Zr-legeringar undersöktes både med hjälp av resistivitetsmätningar och röntgenspektroskopiska mätningar. Kort sagt kan man säga att resistivitetsmätningarna är känsliga för delokaliserade elektroner nära Fermienergin och de spektroskopiska mätningarna är främst känsliga för för hela valensbandet och därmed även för lokaliserade elektroner. På så sätt kan metoderna betraktas som komplementära. Det mest häpnadsväckande resultatet var att det fanns stora skillnader i resistivitetsmätningarna mellan olika kompositioner av Fe/Zr men så gott som inga skillnader i den lokala elektronstrukturen enligt spektroskopiska mätningar. Vi tolkar resultaten som att det finns någon form av aktiveringsbarriär som innebär att elektroner under en viss energi är väsentligt mindre delokaliserade än elektroner med en energi högre än aktiveringsenergin.

2. Introduction

2.1 Ψ

In the theory of quantum mechanics any system is described by its wavefunction, or state, Ψ. Ψ carries all information there is to know about the system. The wavefunction describes the probability of different outcomes during a measurement on the system, such as its spin or position. For example measuring the spin of an electron the spin wavefunction could for example be described as

$$\Psi = \frac{1}{\sqrt{2}}\{|\uparrow\rangle + |\downarrow\rangle\}$$

where the arrows mean spin up and spin down respectively. The expression above describes a situation where a measurement of the spin (in a certain direction) results in either up or down with equal probability. When the spin is measured the wavefunction "collapses" and consists of only spin up or spin down. An electron, which is bound to an atom, is described by its spin wavefunction as well as its spatial wavefunction describing the probability of finding the electron at a point in space. All included in Ψ. Me and my friends, i.e., human beings, generally have difficulties to comprehend concepts like these. What does it mean that a state consists of both spin up and spin down at the same time? Before the spin is measured the question whether the spin is up or down makes no sense, or at least, does not have a simple answer like yes or no. Possibly $\frac{1}{\sqrt{2}}\{|\mathtt{yes}\rangle + |\mathtt{no}\rangle\}$.

In spectroscopy we study transitions between such states and thereby the electronic structure is probed. The electronic structure is closely connected to the properties of atoms, molecules and materials; much like the DNA of an animal is connected to the properties of the animal. However, some (including myself) would claim that properties of atoms are more predictable than properties of biological systems such as yourself.

This thesis contains results from spectroscopic studies of materials relevant for the nuclear industry. The research can be divided in three categories: actinides, copper corrosion and amorphous materials.

3. Nuclear related materials

3.1 Actinides

The nuclear industry is vast. About 6% of the world's energy production is produced by the nuclear industry. In Sweden the same number is about 40%. The basic principle of a nuclear reactor is to split a nucleus (typically ^{235}U and ^{239}Pu) into daughter nuclei by neutron absorption. The daughter nuclei contain less energy per nucleon than their mothers. The excess energy turns into movement of the daughters. Due to the fissile process going on inside a nuclear reactor a build-up of new elements and isotopes occurs continuously. Some of these are radioactive and will decay further. As long as they are radioactive they need to be kept far away from interaction with biological systems. Some isotopes have lifetimes long enough for keeping the fuel radioactive close to 100 000 thousand years. Examples of such are the fission product ^{99}Tc (half-life 220 000 years) and ^{239}Pu (half life 24 000 years) which is formed by neutron absorption. Hence, the danger remains long time after the fuel has been used up. This is why there is a need for a final repository of the spent nuclear fuel. This thesis contains investigations concerning both the potentially hazardous actinides and the copper canister protecting these from entering the environment.

3.2 Copper as material for spent fuel canister

Due to the hazardous properties of the spent nuclear fuel drastic measures need to be taken in order to prevent the material from entering the environment after it has been removed from the reactor. The method needs to keep the material away from biological systems for about 100 000 years. At that time the fission products will have the same level of activity as the natural uranium which was extracted from the mine. In Sweden, the strategy for avoiding such consequences is to put the material in cylindrical canisters which are one meter in diameter and five meters high. They consist of a cast iron inset with square hollow spaces for storage of the spent fuel pellets. Outside the cast iron a five-cm-thick layer of copper constitutes the surface of the canisters. See figure 3.1.

The proposed final repository provides four barriers preventing the material from entering the surrounding. The fuel itself, the corrosion-resistant canister, the bentonite buffer and the surrounding rock mass [1]. The sensitivity

Figure 3.1: Image of sealed (left) and unsealed (right) copper canisters. In the unsealed canister the cast iron inset, which will be inside the copper layer, is visible. The spent nuclear fuel will be stored inside the squared openings in the cast iron. The image is from the Swedish Nuclear Fuel and Waste Management Company, SKB

of X-ray spectroscopies provide opportunities to study the electronic structure of elements in different environments. Hence, it is possible to study what happens to Cu in a certain chemical environment such as the expected environment in the final repository. During the first period the main corrosion process is expected to be oxidation due to molecular oxygen from the air. After the repository has been sealed the molecular oxygen will continuously be consumed by minerals and microbiological activities. When there is no molecular oxygen left sulfur (S) is the most important element still present for chemically harming the surface of the canister. Some studies, though controversial, suggest that copper can corrode in the presence of deionized water [2, 3].

3.3 Amorphous zircaloys

Most solids are crystalline. In mathematical terms a crystal is described by a lattice, i.e., a set of points arranged in a regular pattern of infinite size, mimicking the structure of the real crystal. In turn, the lattice is described by the unit cell which is defined as a unit which is repeated within the lattice. The lattice consists of an infinite number of unit cells located next to each other in three dimensions (normally). The degree of symmetry of the lattice is determined by its point group. The point group determines what symmetry operation that are applicable to the lattice, such as translational, rotational and mirror oper-

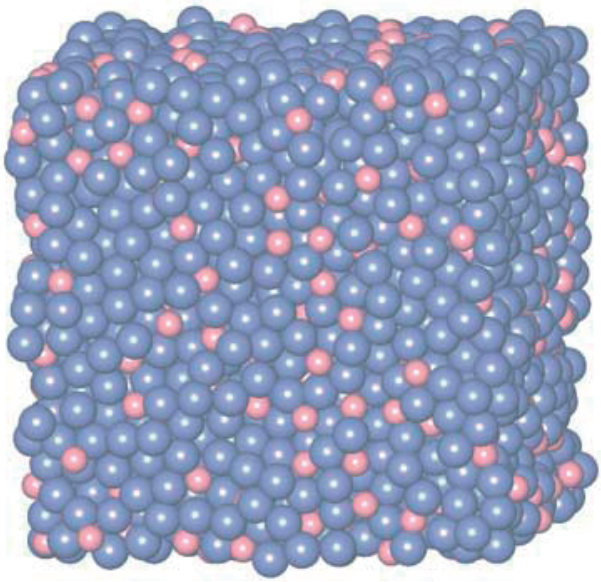

Figure 3.2: Reconstructed model of $Ni_{80}P_{20}$ based on XRD and Fourier transformed EXAFS spectra [4].

ations. A symmetry operation is applicable if the lattice after the operation is indistinguishable from its appearance before the operation.

What has now been described is what amorphous materials are not. An amorphous material might have some degree of local order, but no amorphous material has long range order. Hence, neither translational, mirror operations or any other symmetry operations apply to any description of amorphous materials. Because of the lack of translational symmetry the concept of reciprocal space is difficult to approach. There are for instance no Brillouin zones. Figure 3.2 shows an example of a modeled amorphous structure.

Amorphous metal alloys are interesting materials from both basic and applied points of view. Some have a rich magnetic phase diagram with a Curie temperature tunable with composition [5, 6] and hydrogenation [7, 8]. Some have a high corrosion resistance due to their chemical homogeneity which arises from the random nature of the atomic arrangement. Normally corrosion starts at inhomogeneities such as precipitates and grainboundaries, which are lacking in amorphous structures. See figure 3.3 for a schematic illustration. Amorphous materials are difficult to approach from a theoretical point of view for the reason discussed in the last paragraph. However, using experimental techniques, such as X-ray absorption and emission spectroscopies, the electronic structure is more or less accessible through experiments. The reason why amorphous materials have been investigated in the context of this thesis is their lack of grains and cracks. Inside nuclear reactors, normally corrosion

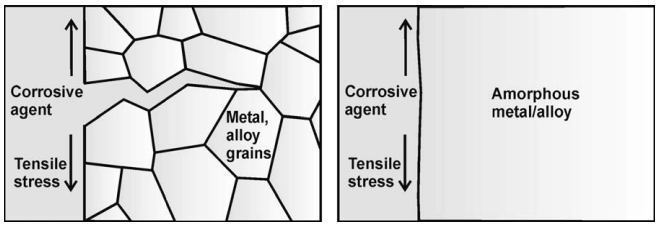

Figure 3.3: Schematic illustration of stress corrosion and cracking [9, 10] A corrosive agent diffuses through the opened crack and corrodes grain boundaries under stress (left image), while the corrosion rate is expected to be different in grain-free materials (right image)

damage occurs due to hydrogen and oxygen penetration through grain boundaries [9, 10]. Hence, these materials are potential candidates to be used in future reactors.

4. Theoretical base for spectroscopy

4.1 Atomic theory

The electronic wavefunction for a stationary system $\Psi(\mathbf{r})$ in a fixed potential $V(\mathbf{r})$ is governed by the Schrödinger equation [11]

$$\left[-\frac{\hbar^2}{2m}\nabla^2 + V(\mathbf{r})\right]\Psi(\mathbf{r}) = E\Psi(\mathbf{r}) \tag{4.1}$$

where m is the mass of the quantum mechanical system (for example an electron) and E is the energy eigenvalue corresponding to the eigenstate $\Psi(\mathbf{r})$. This equation can be solved exactly for the hydrogen atom assuming the nucleus, consisting of one single proton, is fixed in space generating the fixed potential $V(\mathbf{r})$. The potential can be considered as to be time independent since the nucleus is much heavier[1] than the electron and will for that reason be almost fixed in space.[2]

All solutions to equation 4.1 can be expressed in terms of radial functions $R_{nl}(r)$, only depending on the distance r between the nucleus and the electron, and spherical harmonics $Y_{lm}(\theta,\phi)$, only depending on the direction from the origin defined by the angles θ and ϕ.

$$\Psi_{nlm}(r,\theta,\phi) = R_{nl}(r)Y_{lm}(\theta,\phi) \tag{4.2}$$

The subscripts n, l and m are integers defining the particular solution. n is the main quantum number, l is the quantum number corresponding to the orbital angular momentum and m corresponds to the projection of the orbital angular momentum on the z-axis. They are related to each other in the following way:

- $n = 1,2,3,...$
- $l = 0,1,2,...,n-1$
- $m = -l,-l+1,...,-1,0,1,2,...,l-1,l$

It has still not been mentioned that the electron carries spin, s, which is described as an intrinsic angular momentum as opposed to the orbital angular

[1] The proton has 1 836 times larger rest mass than that of the electron [12].

[2] Using the reduced mass, exact solutions of the Schrödinger equation for the hydrogen atom can be obtained by taking into account the movement of the nucleus due to the electric force on the nucleus from the electron. [13] However, this is not conceptually important since the only difference in the equation is that the mass m is exchanged by the reduced mass μ. This modification will not change the behavior of the spatial dependence of the solutions.

momentum l. One electron has $s = 1/2$ and its projection, m_s, on the z-axis is $-1/2$ or $+1/2$. (In this context it is more appropriate to call the projection of the orbital angular momentum m_l instead of simply m.) The spin and orbital angular momentum of one electron can interact and give rise to spin-orbit splittings. This can be seen as multiplet structures of different terms measured by spectroscopic methods. Terms arise from the fact that spin and orbital angular momentum are two components of the total angular momentum j. As long as l and s are proper quantum numbers, terms are defined as ${}^{2S+1}L_J$.

The atomic model, as described so far, works fine as long as the considered system consists of one single electron in a spherically symmetric potential $V(r)$. This is the case for H, He^+, Li^{2+}, Be^{3+}, and so on. However, as soon as there are more than one electron present, the model breaks down. The electrons will interact with each other. In other words the potential, experienced by one of the electrons, is no longer necessarily spherically symmetric.[3] The problem becomes even more apparent in compounds and metals where outer electrons are not only affected by the corresponding nucleus and inner electrons but also by surrounding atoms. It is obvious that spherically symmetric potentials are insufficient in these cases. Even though the radial functions and the spherical harmonics ($R_{nl}(r)$ and $Y_{lm}(\theta,\phi)$) no longer accurately solve the modified Schrödinger equation, they are usually still used as a set of basis for approximate solutions. This is why the terminology inspired by the atomic model remains. s, p and d states, corresponding to states with orbital angular momentum quantum numbers $l = 0$, $l = 1$ and $l = 2$ respectively, are still used to describe valence states in atoms, compounds and metals even though it is not perfectly correct.

4.2 Solid state theory

When approaching new phenomena in quantum mechanics it is usually surprisingly helpful to consider the one-dimensional potential square well. See figure 4.1. Inside the well the potential is zero while outside it is infinite. Solving the Schrödinger equation (equation 4.1) for $\Psi(x)$ the solutions are trigonometric functions with nodes at the walls.

$$\Psi(x) = A\sin(\frac{N\pi x}{b}) \tag{4.3}$$

where A is the amplitude determined from the normalization condition[4], b is the width of the square well and N is a positive integer. Each state corresponds to the energy

[3] Closed shells can in principle be considered as sources of spherically symmetric potentials. Hence, the problem occurs first for the valence electrons.

[4] $\langle\Psi(x)|\Psi(x)\rangle = 1$

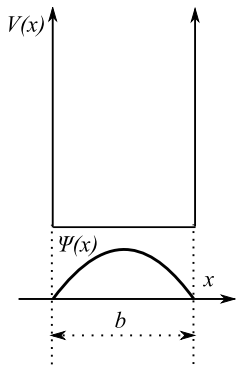

Figure 4.1: The well known state in a square-well potential with infinite walls. The ground state is shown. Not realistic but conceptually important model.

$$E = \frac{\hbar^2 k^2}{2m} \tag{4.4}$$

where $k = N\pi/b$. $k = 2/\lambda$ is the wave number (λ is the wavelength).

Now consider two square wells separated by a finite potential plateau and a finite distance as shown in figure 4.2. The two lowest imaginable states, in terms of energy, are the two states shown in the figure. Which one has the lowest energy? Do they have the same energy? First we realize that higher wave number k means higher energy. See for example equation 4.4. Upon a quick look at the two states Ψ_b and Ψ_a (a stands for bonding and b for anti-bonding state) in figure 4.2 we notice that the wavelength is basically the same for both states, $\Psi_b(x)$ and $\Psi_a(x)$, in the two well regions. However, in the intermediate region in between the wells, $\Psi_a(x)$ has shorter wavelength[5] and hence larger wave number k than that of $\Psi_b(x)$. From this we conclude Ψ_a to have higher energy than Ψ_b [14]. The more the two well regions approach each other the more the wavenumbers of the intermediate region will increase for $\Psi_a(x)$ and decrease for $\Psi_b(x)$. In the limiting case, when the two quantum wells have merged and there is no barrier any more, the situation is again as in figure 4.1. Now $\Psi_b(x)$ corresponds to the ground state in a simple square well potential ($N = 1$) and $\Psi_a(x)$ corresponds to the first excited state ($N = 2$). Now the states are well separated. Compare this to the situation where the two quantum wells are separated by an infinite distance or an infinite potential well. Then Ψ_b an Ψ_a are degenerate. Anything in between these two situations is possible, and any energy splitting between the two states can be achieved by varying the distance between the two wells.

[5] Any periodic function or limited in space can be described as a sum of Fourier components like $\frac{c_0}{2} + \sum_{n=1}^{\infty}[c_n \cos(nx) + d_n \sin(nx)]$.

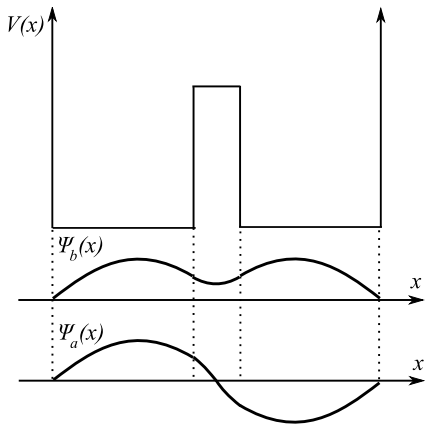

Figure 4.2: A double square-well potential with the two states with lowest energy eigenvalues are shown. Ψ_b stands for the bonding state and Ψ_a for the anti-bonding state.

The energy splitting of two states $\Psi_1(x)$ and $\Psi_2(x)$ is illustrated in figure 4.3. The states $\Psi_1(x)$ and $\Psi_2(x)$ are each almost simple square-well states as shown in figure 4.1 but with a tail entering the barrier with finite potential. They are separated with an infinite distance to each other (but with a finite potential separating them). The figure illustrates the energy splitting occurring as the states approach each other.

Even though the square-well picture is unrealistic and oversimplified the situation does not change fundamentally when for example the H_2^+ ion is investigated. The case can be described as an electron in a potential which is constituted by two fixed "wells", i.e., the protons.[6] Figure 4.3 can just as well be used to illustrate the energy splitting between two protons approaching each other with one common electron. In that case the states Ψ_1 and Ψ_2 would correspond to the $1s$ atomic orbitals of the respective nuclei and Ψ_b and Ψ_a would correspond to the molecular orbitals σ_g and σ_u.[7]

If another square well is added to the previous double-well potential there are three states with similar energies but not degenerate. If more wells are added the energy levels become more and more numerous and closer and closer to each other. In the limit of an infinite number of square wells the levels turn into a continuum. The same goes for atoms, molecules and finally materials. This is why solid state physics is about *bands* as opposed to *discrete*

[6] In the Born-Oppenheimer approximation the protons are assumed to move so much slower than the electrons that they can be considered as fixed in space.

[7] g and u correspond to gerade and ungerade respectively which refer to the molecular wavefunctions which are even (g) and odd (u). Notice the similarity between the square-well situation and the molecular situation.

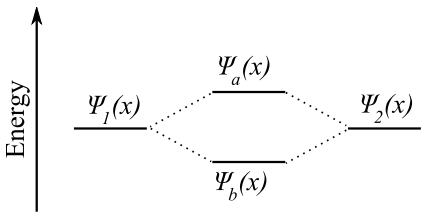

Figure 4.3: Illustration of the energy splitting resulting from two states, Ψ_1 and Ψ_2, approaching each other.

energy levels. We also draw the conclusion that bands become broader the closer together the atoms are situated.

4.3 Transition matrix element

In the field of spectroscopy the relative probabilities of transitions between different states are studied. The probability in question is governed by the matrix element M_{fi} squared. Hence, in spectroscopy we in principle measure the matrix element M_{fi} (squared) corresponding to transitions between the initial state (Ψ_i) and the final state (Ψ_f).

$$M_{fi} = \left\langle \Psi_f \left| \exp(i\mathbf{k}\cdot\mathbf{r})\hat{\varepsilon}\cdot\nabla \right| \Psi_i \right\rangle \tag{4.5}$$

where $\mathbf{k}$ is the wave vector[8] associated with an incident or outgoing electromagnetic wave and $\hat{\varepsilon}$ is the polarization vector.

4.3.1 Dipole approximation

The exponential in the matrix element (equation 4.5) can be expanded with respect to $i\mathbf{k}\cdot\mathbf{r}$ as

$$\exp(i\mathbf{k}\cdot\mathbf{r}) = 1 + (i\mathbf{k}\cdot\mathbf{r}) + \frac{1}{2}(i\mathbf{k}\cdot\mathbf{r})^2 + \ldots \tag{4.6}$$

Considering the argument in the expansion ($i\mathbf{k}\cdot\mathbf{r}$) we notice that if the wavelength of the external wave is much larger than the quantum mechanical system affected by the wave (such as an atom) $\mathbf{k}\cdot\mathbf{r}$ is much smaller than one. Hence, basically only the first term remains in equation 4.6 and the matrix element (equation 4.5) is drastically simplified as

[8]The wave vector $\mathbf{k}$ is the angular frequency of the external electromagnetic wave ω times a unit vector perpendicular to the wave front, i.e., in the direction of the incident wave.

$$M_{fi} = \langle \Psi_f | \hat{\varepsilon} \cdot \nabla | \Psi_i \rangle \tag{4.7}$$

Remembering that $\mathbf{p} = -i\hbar\nabla$, which in turn equals to $m\mathbf{r}$, it can be shown [13] that the matrix element M_{fi} in the dipole approximation can be written as

$$M_{fi} = -\frac{m\omega_{fi}}{\hbar} \langle \Psi_f | \mathbf{r} | \Psi_i \rangle \tag{4.8}$$

The dipole approximation holds very well for optical photons with wavelengths of hundreds of nm compared to atomic distances in the order of Å. The approximation is still appropriate in the soft X-ray energy range (up to a few hundred eV and a few nm) but at a few keV other terms in the expansion starts to become significant.

5. X-ray spectroscopic techniques

A photon with wavelength λ has a certain probability to successfully pass through a piece of material of a certain thickness l. Hence, the absorption of photons in a piece of material is decaying exponentially with respect to l. Given a piece of material and a photon wavelength there is a given attenuation length, i.e., the distance where $1/e$ fractions of the original flux penetrates the material. For 1 keV the penetration depth is typically 0.1 μm and a few μm for 10 keV. These length scales illustrates the fact that X-ray spectroscopies are bulk sensitive compared to electron spectroscopies with attenuation lengths of a few Å. This makes X-ray spectroscopies a suitable method for $in-situ$ experiments where actual chemical processes can be studied as they happen.

5.1 X-ray absorption spectroscopy

X-ray absorption spectroscopy (XAS) is illustrated in figure 5.1. An incident photon excites an electron from an inner core level of an atom. The transition rate in XAS is proportional to the matrix element squared and inversely proportional to ω_{fi}^2 and, hence,

$$I_{abs}(\omega) \propto \left|\left\langle \Psi_f \left| \hat{\varepsilon} \cdot \mathbf{r} \right| \Psi_i \right\rangle\right|^2 \delta_{E_f - E_i - \hbar\omega} \tag{5.1}$$

where I_{abs} is the absorbed intensity of the incoming photon beam and $\delta_{E_f - E_i - \hbar\omega}$ makes sure the energy is conserved in the system. Shortly after an X-ray photon has been absorbed the excess energy is used to emit secondary electrons or other photons. Emission of secondary electrons is the most common process in the X-ray energy scale. The amount of secondary electrons emitted is proportional to the amount of absorbed X-ray photons. Hence, the current on the sample can be used as a measure of the absorption coefficient. This method is called XAS in the total electron yield (TEY) mode. Similarly the amount of emitted photons is proportional to the degree of absorption of X-ray photons. Measuring XAS by counting the number of photons emitted (independently of their energy) is called XAS in the total fluorescence yield (TFY) mode. The incident energy is continuously varied and the intensity recorded (electrons or photons) at each incident energy. A spectrum is generated.

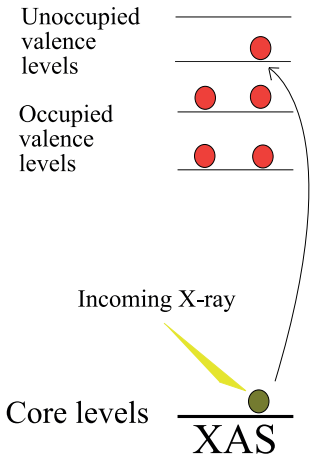

Figure 5.1: Schematic illustration of X-ray absorption spectroscopy.

The spectrum corresponds to a convolution of the core-electron energy level and the unoccupied states in the valence band where to electrons can be excited. Since the energy of the core-electron is element specific so is XAS. The electronic structure of specific elements can be studied. Since the dipole approximation usually applies in our experiments the method is also orbital specific. The partial unoccupied density of states is probed.

5.2 X-ray emission spectroscopy

X-ray emission spectroscopy (XES) is illustrated in figure 5.2. After a photon has been absorbed it has already been mentioned that secondary electrons and photons are emitted from the excited atom in the de-excitation process, i.e., when the previously formed core hole is being filled by an electron. When the energy of outgoing photons are measured we call it XES. In XES occupied states are probed. Again the dipole approximation applies (usually) and again the method is element specific since it is based on the core energy levels of a specific element. As a result, the occupied density of states is probed.

XES is a photon-expensive process in the sense that it takes very many photons per measured photon. This is because the cross-section for photon emission is much less than the cross-section of the Auger decay[1] and due to the small solid angle of collected photons emitted from the sample.

One advantage of XES (in comparison to XAS) is that the incidence energy can be tuned to resonantly excite a certain state in the system investigated.

[1] Auger decay is the process where one electron fills a core hole and another shallow electron is emitted.

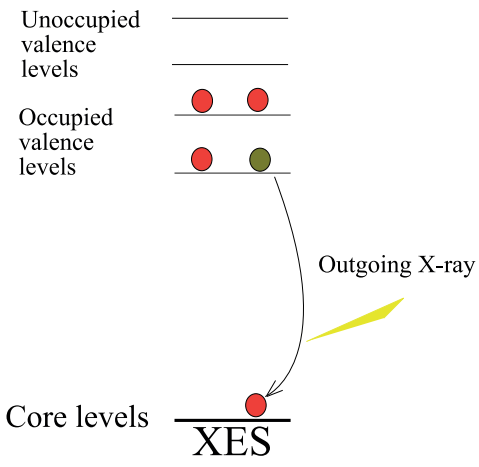

Figure 5.2: Schematic illustration of X-ray emission spectroscopy.

The particular state can then be studied separately by tuning the incoming energy as to amplify transitions associated with the state of interest. The state could be an atom with a different oxidation state than other atoms of the same element in the studied system, or it could be an inequivalent site [15]. Hence, XES is not only element and orbital selective, but also site selective.

The following example is used to illustrate the usefulness of XES in terms of selectivity.

Sulfur can be in many different oxidation states from S(-II) to S(VI). One of the good examples is sodium thiosulfate $Na_2S_2O_3$. The thiosulfate group consists of two sulfur atoms and three oxygen atoms as illustrated in figure 5.3. The thiosulfate group is almost identical to the sulfate group consisting of one sulfur atom and four oxygen atoms. The difference is that one of the oxygen atoms in the sulfate group has been replaced by a sulfur atom in the thiosulfate group. In the sulfate group the oxidation state of the S atom is S(VI) and the oxidation state of every oxygen atom is O(-II). Since it is possible for S to be in oxidation state S(-II) we guess that the sulfur atom in thiosulfate, solely bonding to the central sulfur atom, is in the oxidation state S(-II). Hence, we have a system with two S atoms with completely different oxidation states and, thus, different electronic environments. Using XES the electronic structures of the two S sites can be studied separately as is shown below.

Figure 5.4 displays S $L_{2,3}$ X-ray absorption spectra of sodium sulfate Na_2SO_4 and sodium thiosulfate $Na_2S_2O_3$. The absorption edge of S in sodium sulfate starts at $\sim$171 eV as can be seen in figure 5.4. (The structures at lower energies do not belong to S.) The absorption edge of S in sodium thiosulfate starts at $\sim$ 161 eV as can be seen in the spectrum of sodium thiosulfate. This spectrum has features all the way from $\sim$161 eV to $\sim$185 eV with structures above 171 eV resembling those of the spectrum of sodium

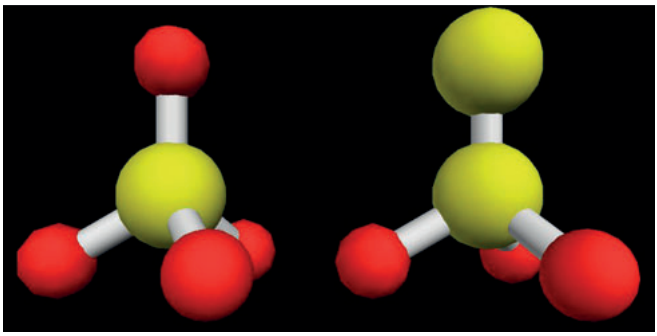

Figure 5.3: Illustration of sulfate $SO_4)^{2-}$ (left) and thiosulfate $(S_2O_3)^{2-}$ (right) ions. Yellow spheres represent sulfur atoms and red spheres represent oxygen atoms.

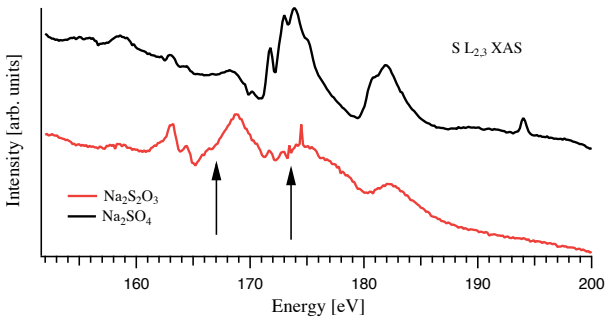

Figure 5.4: S $L_{2,3}$ X-ray absorption spectra of sodium sulfate Na_2SO_4 and sodium thiosulfate $Na_2S_2O_3$. The excitation energies used for the X-ray emission spectra are indicated by arrows.

sulfate. The features below 171 eV belong to S(-II) while the structures above 171 eV can be a combination of the S(VI) and S(-II) sites.

In X-ray emission spectroscopy one excitation energy is chosen. If the excitation energy is less than the absorption edge of S in sodium sulfate, i.e., below 171 eV only S(-II) sites will be excited and the emission spectra will only reflect the electronic structure of S(-II) sites. Figure 5.5 shows X-ray emission spectra of sodium thiosulfate $Na_2S_2O_3$, calcium sulfate Ca_2SO_4, and sodium sulfide Na_2S measured at two different excitation energies. Calcium sulfate and sodium sulfide represent S(VI) and S(-II) respectively while sodium thiosulfate presumably represents both. For the excitation energy 167 eV the spectrum of sodium thiosulfate is compared to that of sodium sulfide and the resemblance is clear, confirming that sulfur in sodium thiosulfate has a S(-II) component. For the excitation energy 173.5 eV the spectrum of sodium thiosulfate is compared to that of calcium thiosulfate. New structures arising at $\sim$155 and $\sim$161 eV in the spectrum of sodium thiosulfate are found to be

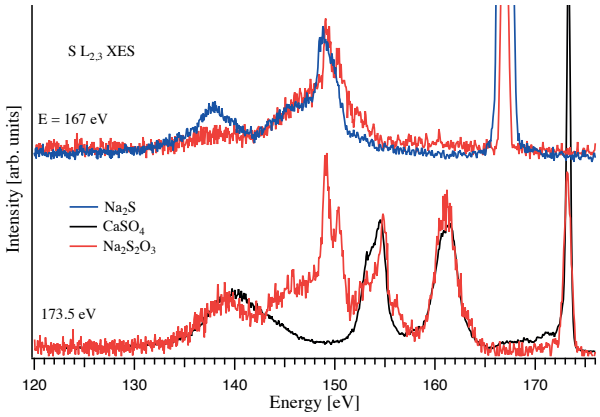

Figure 5.5: S $L_{2,3}$ X-ray emission spectra of sodium thiosulfate $Na_2S_2O_3$, calcium sulfate Ca_2SO_4, and sodium sulfide Na_2S. Excitation energies are indicated.

at the same positions as those of calcium sulfate. This spectrum of $Na_2S_2O_3$ contains contributions from both S(-II) and S(VI).

5.3 Resonant inelastic X-ray scattering

Resonant inelastic X-ray scattering (RIXS) is often viewed as a a combination of absorption and emission [16]. In the process of RIXS a core electron is excited into an unoccupied valence level. The system is excited and de-excited within typically a few femtoseconds. Note that the charge of the system is unchanged during the process, i.e., no electron is lost or added. The cross-section of the whole process is determined by the square of the sum of the probability amplitudes of all excitation-emission paths, as described by equation 5.2 [17].

$$I_{RIXS}(\omega_{abs},\omega_{em}) \propto \sum_f \left| \sum_c \frac{\langle \Psi_f | \hat{e}_{em}\cdot\mathbf{r} | \Psi_c \rangle \langle \Psi_c | \hat{e}_{abs}\cdot\mathbf{r} | \Psi_i \rangle}{E_i + \omega_{abs} - E_c - i\Gamma_c} \right|^2 \delta_{E_f+\hbar\omega_{em}-E_i-\hbar\omega_{abs}} \tag{5.2}$$

where subscripts i, c and f denote initial, intermediate and final states respectively. Subscripts *abs* and *em* mean that the corresponding quantity is associated with the absorption and emission processes respectively.

This is an excellent example of the peculiar consequences of quantum mechanics in the following sense: in one single RIXS process all excitation-emission paths give contributions to the probability of that process to occur, as if they all occurred at the same. The states Ψ_c can be considered as virtual intermediate states which are all present in the sense that they all affect the total cross-section of the process.

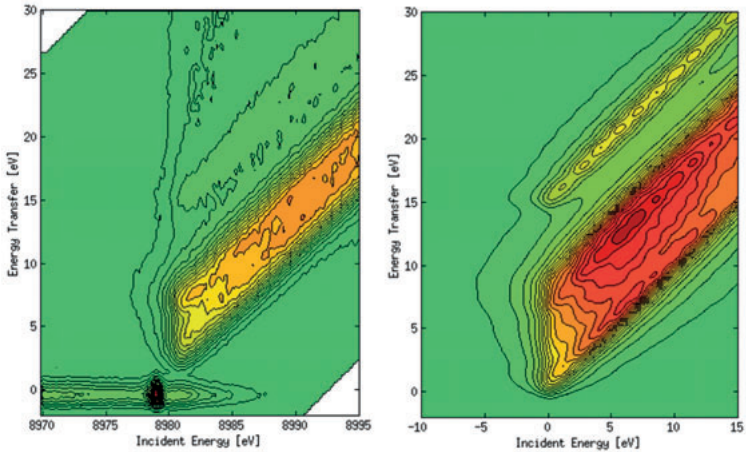

Figure 5.6: RIXS map of Cu_2S at the Cu K edge. The measured map (left) is compared to the calculated one (right).

RIXS depends on both incoming and outgoing photon energies why the full RIXS picture is two-dimensional. The measured intensity depends on incident and outgoing energies. This is illustrated in figure 5.6 where measured and calculated RIXS intensities are plotted as a function of incident energy and energy transfer (difference between incident and outgoing energies, i.e., energy loss). The particular example is measurements and calculations for Cu_2S at the Cu K edge performed at the beamline ID26 at the ESRF in Grenoble, France. The horizontal structure at the bottom of the left figure represents the elastic peak which is at zero eV energy transfer. Other horizontal structures would correspond to resonant inelastic scattering, typical RIXS process. The general trend in this case is that the structures (other than the elastic peak) are receding from the elastic peak. However, this does not exclude contributions from structures at constant energy transfer within the seen structures.

In XAS the presence of a core hole in the final state gives rise to a broadening due to the short life time of the formed state, typically a few femtoseconds as mentioned earlier. In the RIXS process the core-hole state is an intermediate state instead, i.e., it is a virtual state. Hence, the life-time broadening is removed. In XAS usually the core-hole life-time broadening is the limiting factor in terms of resolution. In RIXS usually the experimental resolution is the limiting factor. This provides new opportunities to improve resolutions which are not governed by nature.

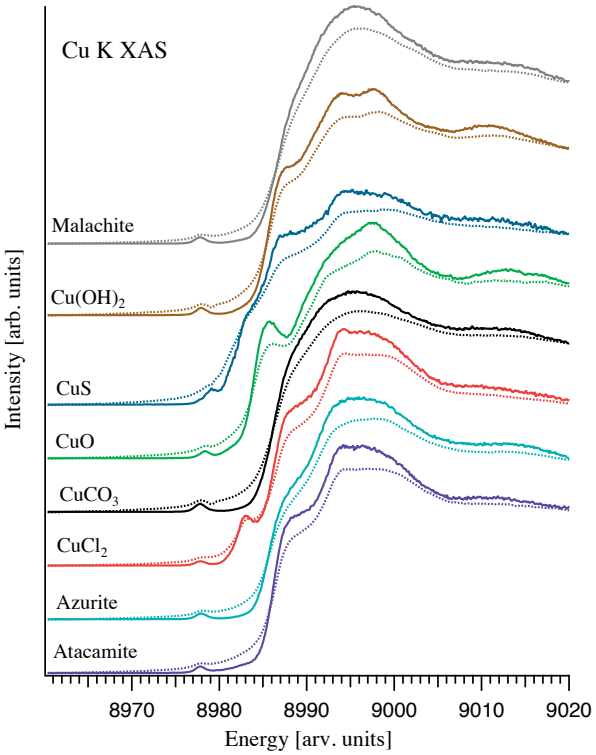

Figure 5.7: Cu K XAS spectra of divalent Cu compounds. Dashed and solid lines correspond to measurements in TFY and HERFD modes respectively.

5.4 X-ray absorption spectroscopy in the high energy resolution fluorescence detection mode

The core-hole life-time broadening present in XAS measurements can be significantly reduced by measuring XAS in the high energy resolution fluorescence detection (HERFD) mode. The life-time of the observed state is increased by selecting only one transition associated with a life-time which by necessity is longer than the total life-time of the excited state. This is done by putting the spectrometer as to select only one emission energy while the incident energy is changed continuously. This can be done at the beamline ID26 at the ESRF for example. A description of the stationary spectrometer follows in the section below.

Figure 5.7 shows Cu K XAS spectra of divalent Cu compounds in the TFY (dashed lines) and HERFD (solid lines) modes. Structures in the HERFD-XAS spectra are more pronounced, especially at the pre-edge (8975-8980 eV) present in all spectra of divalent Cu compounds. The pre-edge corresponds

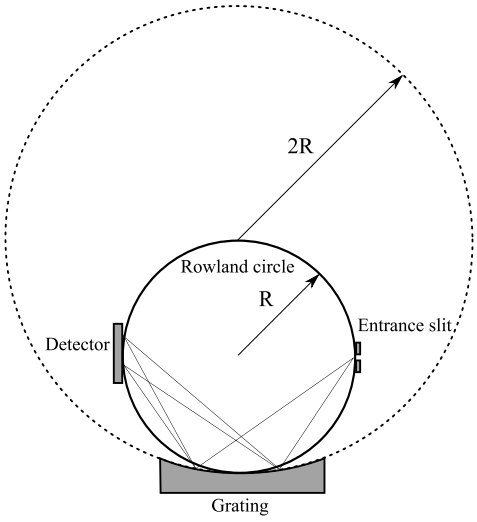

Figure 5.8: Illustration of the Rowland geometry. Two rays of different wavelengths are indicated with thin lines hitting the detector at two points corresponding to their respective energies.

to quadrupole Cu 1*s* - 3*d* transitions.[2] This structure is a sign of presence of divalent Cu. The oxidation state of Cu in copper sulfides is under debate. Some consider Cu to be monovalent in all copper sulfides, including CuS. However, using XAS in the HERFD mode we observe significant contribution from 1*s*-3*d* transitions of Cu indicating presence of divalent Cu in CuS as seen in figure 5.7

5.5 Spectrometers

In the present work two different spectrometers have been employed. They both make use of the Rowland circle geometry. The principle is simple. Light of possibly different wavelengths enter through the entrance slit. The incoming beam covers a certain area of the grating and it scatters. The scattering angle depends on the incoming angle and the wavelength. Rays of a certain wavelength will meet each other on the rowland circle in a certain point (assuming plane geometry). Hence, different points on the detector corresponds to different energies. This provides the opportunity to study energy-resolved intensities of emitted light. See figure 5.8 for schematic illustration.

[2]Quadrupole transitions are suppressed due to the dipole selection rules but at these energies the dipole approximation is less strict and significant contributions from quadrupole transitions can be observed.

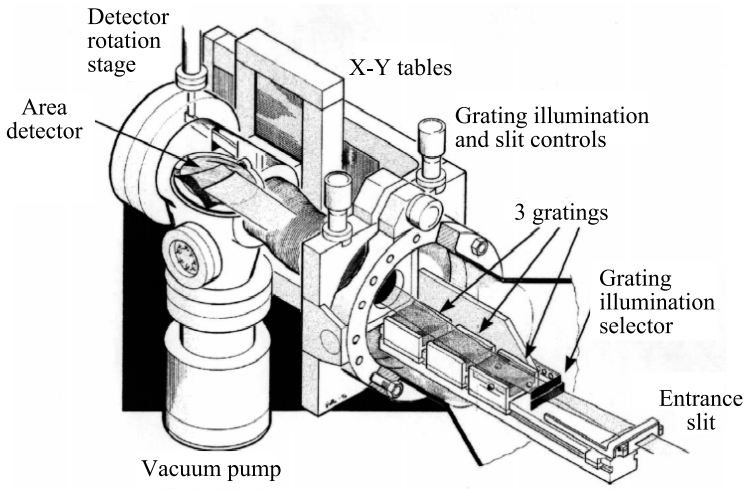

Figure 5.9: A drawing of the grazing-incidence spectrometer designed by Nordgren [18].

5.5.1 Grazing-incidence spectrometer for soft X-rays

During the spectroscopic experiments using soft X-rays (50-1000 eV) a portable grazing-incidence spectrometer has been employed for X-ray emission measurements, designed by Nordgren [19]. Figure 5.9 shows a drawing of the instrument. The important part is the entrance slit close to the sample. The sample is illuminated by the radiation generated by preferably a synchrotron. The purpose of the entrance slit is to create a source smaller than the illuminated spot on the sample and by that manner improve the resolution. By making the entrance slit smaller the number of photons coming through decreases. This is a trade off: flux versus resolution. In this context it should be emphasized that if the spot on the sample is very small, typically 10 μm (vertically) the slit can be removed and slit-less experiments can be performed with high flux and high resolution. Three gratings with different groove densities and radii provide a large energy range (50-1000 eV). The grating is selected by the grating illumination selectors. The two-dimensional area detector is a micro-channel plate (MCP) which consists of a surface filled with micro channels. When a photon gets absorbed in a channel, electrons are emitted. The emitted electrons are guided through the micro channel by a potential. The signal gets multiplied and finally hits a fluorescent material which emits optical light detectable by an ordinary camera. The area detector is positioned as to tangent the Rowland circle where rays corresponding to one energy are focused. The positioning is controlled by the X-Y tables. Compare figures 5.8 and 5.9 and compare the positions of the entrance slit and the detector.

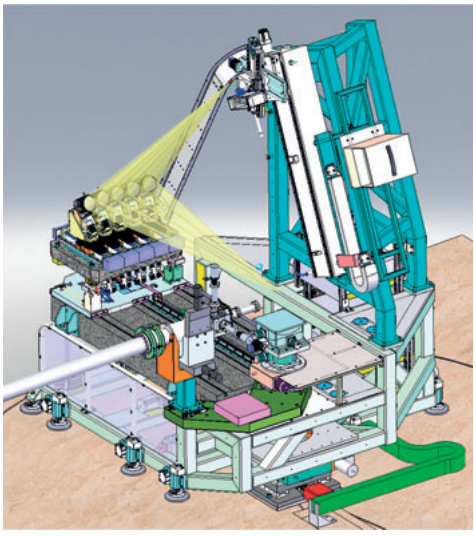

Figure 5.10: Crystal analyzer for emission measurements with hard X-rays.

5.5.2 Crystal analyzer spectrometer for hard X-rays

Spectroscopic experiments using hard X-rays (2.5-30 keV) were performed at beamline ID26 at the ESRF using an X-ray emission spectrometer [20]. The lattice constant (distance between the grooves) of a grating needs to be in the order of the wavelength of the associated photons. In hard X-rays the lattice constant is approaching atomic distances. Hence, crystals are used instead of gratings. A bent crystal reestablishes the Rowland geometry. The detector on the Rowland circle is a linear solid-state detector which only records one energy at the time (compare to the two-dimensional MCP detector in the previous section). The setup facilitates the simultaneous usage of five bent crystals in order to increase the solid angle collection of photons emitted from the sample.

6. Results

6.1 PuO_2 oxidation

It has recently been found that PuO_2 can form higher Pu oxidation states by reaction with water [21]. Pu with higher oxidation state than Pu(IV) has a higher solubility generating consequences for the proposed underground repository of spent nuclear fuel.

Due to the hazardous properties of Pu, safety restrictions on international research facilities, such as synchrotrons, make it difficult to perform important experiments on such systems. Therefore, we developed a closed-source experimental setup allowing for X-ray spectroscopic studies of Pu systems under safety restrictions. A detailed description of the experimental setup is given in Paper II and the scientific results are presented in Paper III.

O K absorption and O Kα ($2p$ - $1s$ transitions) emission spectroscopy experiments were performed on the single-crystal PuO_2 sample (^{239}Pu) as the closed source, and on the polycrystalline PuO_2 sample (^{242}Pu) as an open source. Reasonable agreement between the spectra were found, confirming the efficiency of the closed-source experimental setup. Different spots on the surfaces of both samples were probed and the same spectral features were present in all spectra. However, the relative intensities of especially the two features at $\sim$2 eV and $\sim$5 eV of different spots varied. The feature at $\sim$2 eV had the highest intensity on the single crystal.

Generalized gradient approximation (GGA) calculations accounting for the coulomb-interaction U (GGA+U) were performed for further analysis of the spectroscopic data. Based on results from the calculations we conclude that structures at $\sim$2 eV and $\sim$5 eV arise from O $2p$-Pu $5f$ and Pu $6d$ hybridizations respectively. Thus, different degrees of oxidation are expected to influence the structure at $\sim$2 eV.

The O K XA spectra of the single crystal were compared with appropriately broadened O $2p$ states in order to establish a suitable value of the Hubbard parameter U as shown in the upper panel of figure 6.1. The best agreement in terms of peak positions and relative intensities was achieved for U=5 eV. This value was used in the further analysis. Previous X-ray spectroscopic studies indicate fractional contribution from Pu in higher oxidation states than Pu(IV) in polycrystalline sample [22]. O K edge X-ray absorption spectra were also calculated for different defect structures which lead to different degrees of Pu $5d$ population. The results are shown in the lower panel of figure 6.1.

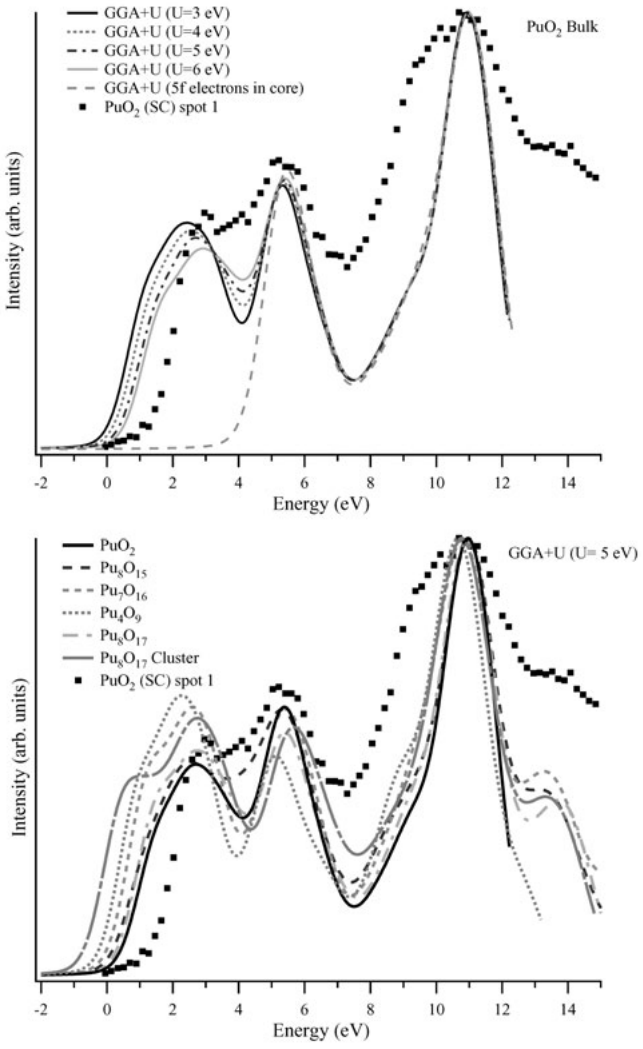

Figure 6.1: Simulated O K X-ray absorption spectra based on GGA+U calculations are shown in the upper panel together with the measured sample of the single crystal (SC) PuO_2 sample. The lower panel shows GGA+U based calculations of O K X-ray absorption spectra of defect structures together with the spectrum of the single crystal PuO_2 sample.

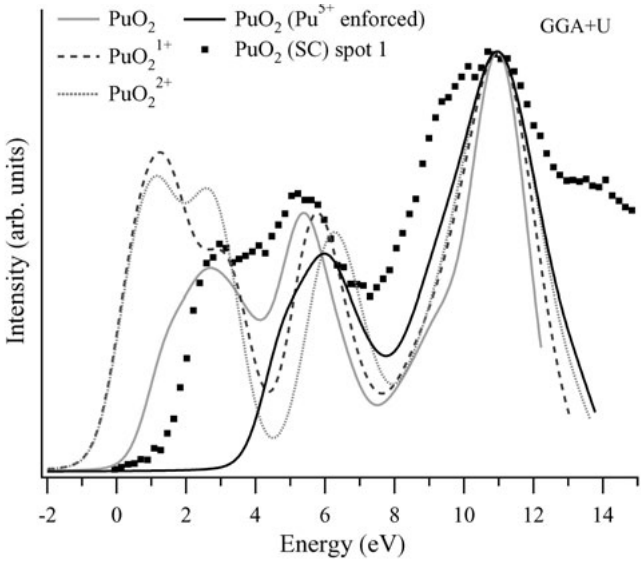

Figure 6.2: Simulations of X-ray absorption spectra based on GGA+U calculations for Pu(V) systems: PuO_2^{1+}, PuO_2^{2+} with U=5 eV and PuO_2 with enforced Pu(V) using U=22 eV along with measured X-ray absorption spectrum of single crystal (PuO_2).

As seen in the lower panel of figure 6.1 the trend is that the intensity of the structure at $\sim$2 eV of the calculated spectra becomes more pronounced with formally decreasing Pu $5f$ population. See for example the calculated spectrum of Pu_4O_9. This is the opposite to what is observed in experiment since the polycrystalline sample which has a fraction of Pu in higher oxidation states than Pu(IV) shows the least pronounced structure at $\sim$2 eV. A plausible explanation to such a behavior could be that Pu sites in the GGA+U calculations are nearly equivalent while the polycrystalline sample can be viewed as a system containing inequivalent Pu sites with $Pu^{(IV)}O_2$ and $Pu^{(V)}O_2$.

O K X-ray absorption spectra of Pu(V) sites were simulated using GGA+U calculations in different ways as shown in figure 6.2. For PuO_2^{1+} and PuO_2^{2+} the value of U was set to 5 eV. Pu(V) was enforced by putting U=22 eV to prevent relaxation. Using linear combinations of the spectrum of the enforced Pu(V) calculation and the spectrum of the $Pu^{(IV)}O_2$ a series of spectra with different contributions of Pu(V) fraction was constructed and presented in figure 6.3. The linear combination was constructed according to equation 6.1. The best agreement with experiment was reached for α values between 4.050 and 4.125, thus suggesting presence of an $\sim$8% fraction of Pu(V) in the polycrystalline sample.

$$Pu^{(4+\alpha)}O_2 = \alpha Pu^{(V)}O_2 + (1-\alpha)Pu^{(IV)}O_2, \tag{6.1}$$

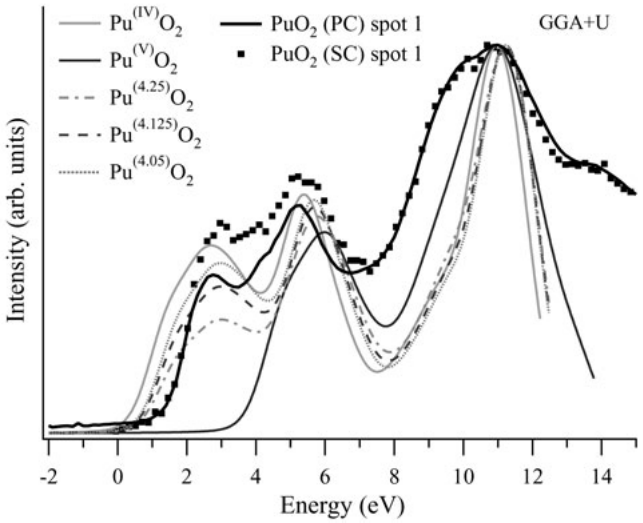

Figure 6.3: Simulated O K X-ray absorption spectra using GGA+U calculations for stoichiometric PuO_2, PuO_2 with enforced Pu(V) and linear combinations of the two, together with experimentally recorded spectrum of the single crystal and the polycrystalline samples.

where α is the fraction of $Pu^{(V)}$.

6.2 Se(IV) reduction

The radionuclide ^{79}Se is one of the daughter products present in the spent nuclear fuel. The fraction of ^{79}Se is only $\sim$0.04% at the end of the fuel cycle but its halflife (1.1 million years) and its potentially high mobility makes it into an important issue concerning the final repository of spent nuclear fuel.

Selenium can exist in several different oxidation states, Se(-II), Se(0), Se(IV) and Se(VI) (compare to sulfur as described in the previous chapter). The selenate, Se(VI), is the dominating specimen under oxidizing conditions and it shows high mobility in soils and groundwaters. Selenium in lower oxidation states is less mobile due to lower solubility. The interior of a final-disposal canister consists of cast iron inset which at some point can be exposed to groundwater. Thus, a key concern regarding Se is how its oxidation state behaves in groundwater in contact with Fe.

The experiment is described in detail in Paper IV. Two samples were prepared. The steel foil was polished and put in groundwater solution with selenate ions, $(SeO_4)^{2-}$. A second iron sample was pre-oxidized and afterwards put in groundwater solution with selenate ions. The two pieces were dried and studied by means of X-ray absorption spectroscopy (XAS) in the high energy

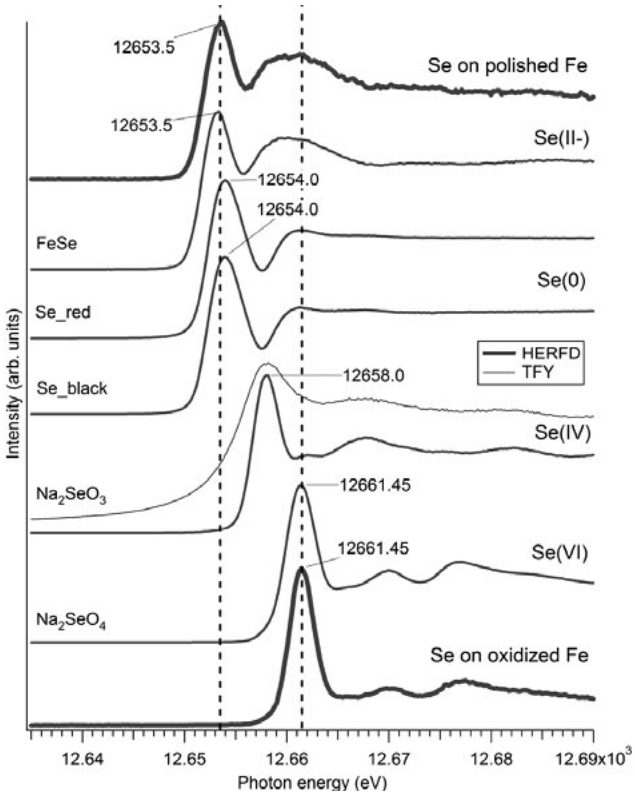

Figure 6.4: High energy resolution fluorescence spectra of Se model systems and Fe films exposed to groundwater solution and selenate ions.

resolution fluorescence detection (HERFD) mode. In this case the intensity of the Se Kα_1 emission line was measured as a function of the incoming energy. X-ray absorption spectra of model compounds were also measured with the same technique. The samples were FeSe, red Se, black Se, Na_2SO_3 and Na_2SO_4 representing different oxidation states of Se. The results are shown in figure 6.4.

The absorption spectrum of the sample with pre-oxidized Fe resembles that of Se(VI), while the spectrum of the sample with polished Fe surface resembles that of Se(-II), thus, indicating a reduction of Se had taken place in contact with the polished Fe surface. Thereby, we conclude that the degree oxidation of the Fe in the iron inset in the final-disposal canisters is an important factor for the risk of Se spreading in the surrounding environment of the repository layout.

6.3 Copper corrosion

The spectroscopic data for copper systems presented here cover a large energy range from the S $L_{2,3}$ edge ($\sim$150 eV) to the Cu K edge ($\sim$9000 eV). The experiments were performed at MAX-lab, Lund and at the ESRF, Grenoble.

6.3.1 Copper sulfidation

In the study of copper corrosion in the expected environment of the underground repository of spent nuclear fuel in Sweden, the role of sulfur is of main importance due to the lack of molecular oxygen. We here present a method to distinguish between the two copper sulfides Cu_2S and CuS formed on the surface of a piece of copper. Sulfides are the final products in the sulfidation of Cu in oxygen-free environments. The details of the following experiment can be found in Paper V.

It is sometimes challenging to study a thin sulfide film which has formed on the surface of a piece of copper using spectroscopic measurements at Cu edges. If the film is thin enough, the recorded data will mainly represent metallic copper from underneath the sulfide film due to the relatively large attenuation length of X-rays. We present results for a thin sulfide layer on the surface of a copper foil obtained by means of S $L_{2,3}$ XES measurements. Since we study a S edge there is no contribution from the Cu bulk. Only from the sulfide film. As seen in figure 6.5 there is a significant difference between S $L_{2,3}$ XES spectra of the two sulfides Cu_2S and CuS. The spectrum of CuS is significantly broader than that of Cu_2S. The origin of the broadening is the atomic structure of CuS which has two inequivalent S sites giving rise to different states in the valence band. There is also a chemical shift between the two sites which have been accounted for in the simulated spectrum of CuS.

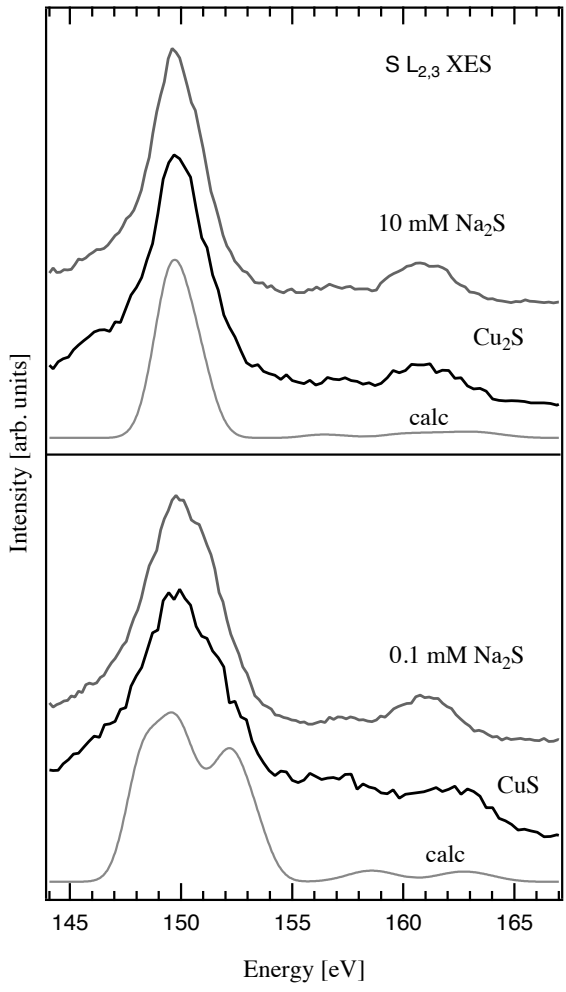

Figure 6.5: S $L_{2,3}$ XES spectra of CuS, Cu_2S and Cu foils exposed to the solutions with different concentrations of Na_2S. The concentrations are indicated in the figure. The excitation energy was 174 eV.

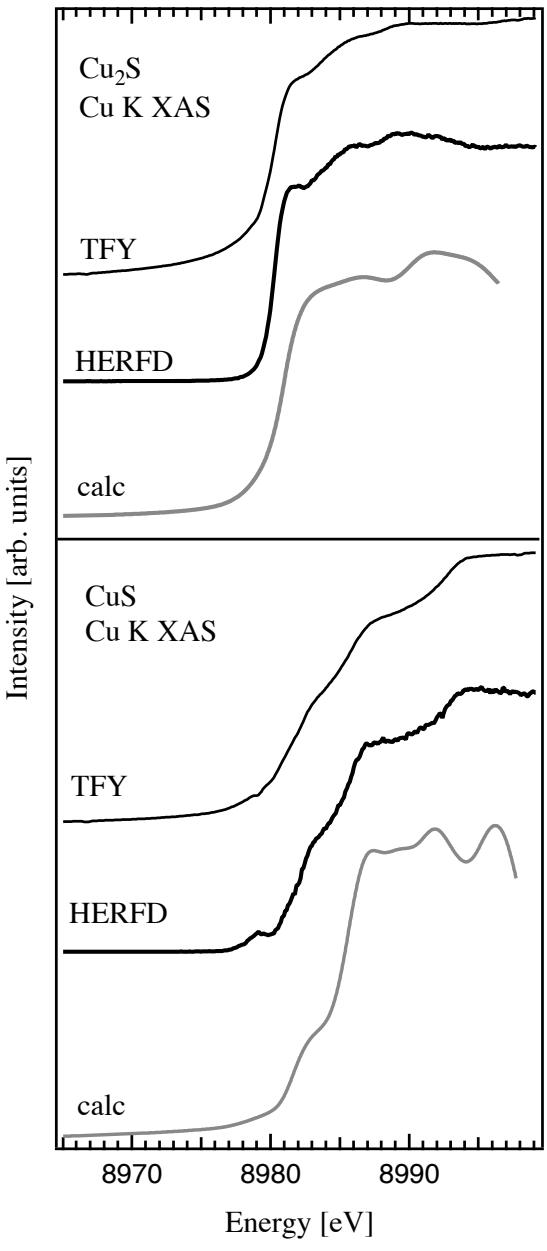

Figure 6.6: Cu K XAS spectra of Cu_2S and CuS measured in both TFY (black thin curve) and HERFD (black thick curve) modes. Simulated spectra using LDA-calculated Cu 4*p* DOS are also shown (red curves).

The most common opinion is to consider copper sulfides as monovalent copper compounds, i.e., Cu(I) [23, 24]. However, some [25, 26] suggest a more complex situation and possible presence of Cu(II). Cu K XAS spectra mainly represent transitions from $1s$ to $4p$ of Cu. (See figure 6.6.) All divalent copper compounds have a pre-peak signifying quadrupole transitions from $1s$ to $3d$ states of Cu since divalent copper compounds have the electronic configuration [Ar]$3d^9$ and, hence, unoccupied $3d$ states in the valence band. The structure is strongly suppressed due to dominance of the dipole approximation but it is still significant because of the short wavelengths involved X-rays ($\sim$9000 eV) which make the dipole selection rules less strict.

Measuring the intensity of the $3p$ to $1s$ transitions as a function of incident energy, i.e., XAS in HERFD mode, the spectral broadening due to the short lifetime is significantly reduced and the quadrupole pre-peak becomes more resolved. The pre-peak is present in CuS indicating the existence of unoccupied $3d$ states in the valence band, thereby supporting the theory that Cu in CuS is not simply Cu(I).

We studied a thin copper film exposed to Na_2S solution using Cu K XAS in HERFD mode. We found that the integrated Cu signal decreased as a function of time as shown in figure 6.7. After modeling the behavior the situation was best described by Cu entering the solution. However, considering the low solubility of copper sulfides the explanation that the copper sulfides are dissolved in the solution is not satisfactory. Our tentative explanation is that the beam creates free radicals via radiolysis of the water. The free radicals oxidize S from S(-II) as in sulfides to S(IV) and S(VI) as in sulfites and sulfates which have a solubility tremendously higher than that of sulfides.

In Paper VI we demonstrate, using Cu $L_{2,3}$ and O K X-ray absorption and emission spectroscopies, that thermally formed divalent Cu, Cu(II), is efficiently reduced to Cu(I) after exposure to Na_2S solution. Figure 6.8 shows data representing Cu $L_{2,3}$ X-ray absorption measurements of monovalent and divalent Cu, and monovalent and divalent Cu exposed to Na_2S solution. The spectrum of Cu(II) contains a strong structure at $\sim$931 eV representing transitions from Cu $2p_{3/2}$ to $3d$ states because of the $3d^9$ character of divalent Cu compounds and, hence, unoccupied $3d$ states. This feature is not present in the spectrum of Cu(I) and neither in the spectrum of Cu(II)+Na_2S. This indicates that divalent Cu is reduced after exposure to Na_2S solution.

6.3.2 Monovalent copper compounds

In the debate concerning copper corrosion in oxygen free water [2, 3, 27, 28] Cu-O-H phases of Cu(I) are proposed as intermediate stages in the corrosion process. Hence, the importance of experimental methods for distinguishing between different monovalent Cu compounds has become an important issue.

Divalent Cu compounds have a $3d^9$ electronic configuration. Since the $3d$ band is unfilled, $3d$ electrons of Cu in the valence band are responsible for

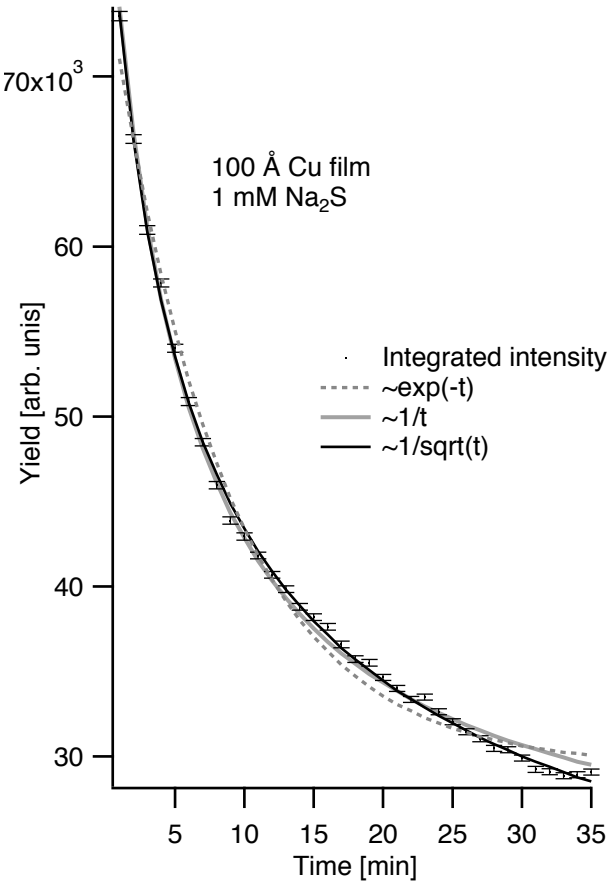

Figure 6.7: The integrated Cu K XAS signal in the HERFD mode is shown as a function of time with estimated error bars corresponding to one standard deviation. Three calculated curves correspond to the three discussed in the text. Formation of 2D islands (red dashed line), thermal diffusion (green solid line) and diffusion into the solution (black solid line).

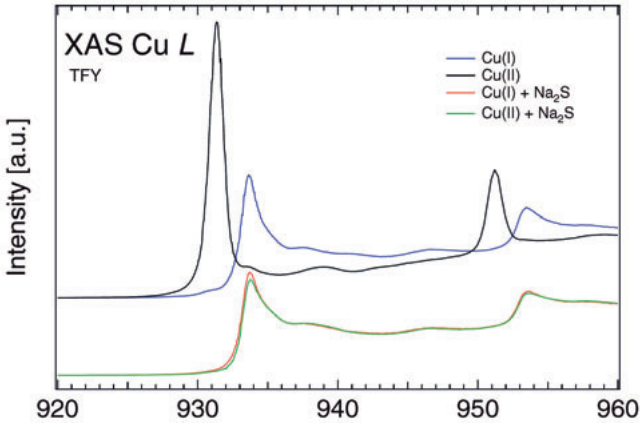

Figure 6.8: Cu $L_{2,3}$ XAS spectra of thermally generated monovalent and divalent Cu oxides (Cu(I) and Cu(II)) and the same samples exposed to Na_2S solution.

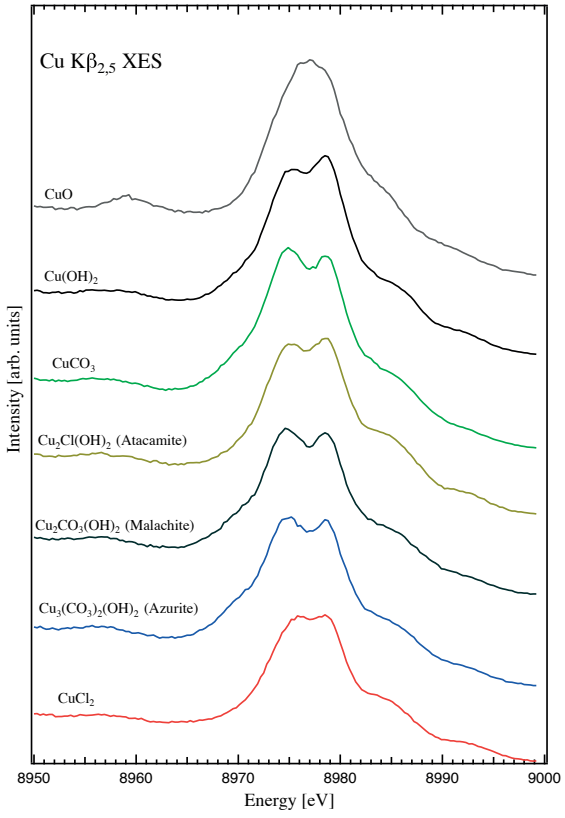

Figure 6.9: Cu K$\beta_{2,5}$ X-ray emission spectra of divalent Cu compounds.

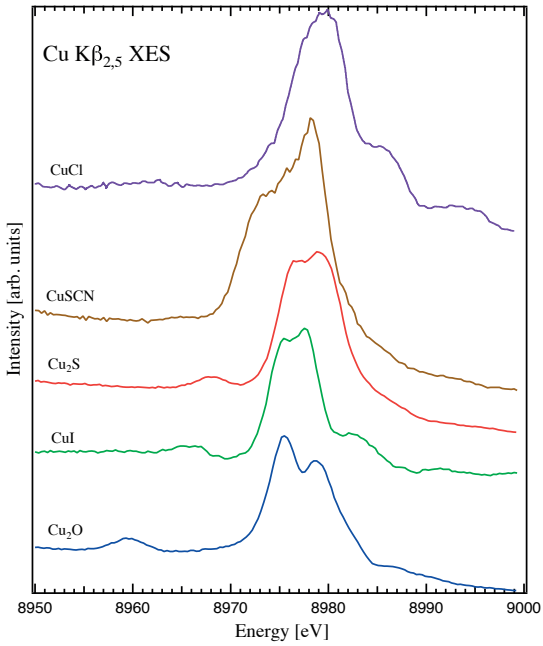

Figure 6.10: Cu K$\beta_{2,5}$ X-ray emission spectra of divalent Cu compounds.

the chemical bonding in such compounds. On the other hand monovalent Cu compounds have a $3d^{10}$ electronic configuration. Since the $3d$ band is filled, $4s$, p states of Cu become important. This can be illustrated using Cu K$\beta_{2,5}$ X-ray emission spectroscopy since it probes the $4p$ states of Cu. This was done in Paper VII.

Figure 6.9 shows the results of Cu K$\beta_{2,5}$ X-ray emission measurements for divalent Cu compounds. The similarity between the spectra is in line with the anticipation that the Cu $4p$ states are not the important states for the chemical bonding in these systems. Figure 6.10 displays the Cu K$\beta_{2,5}$ X-ray emission spectra of monovalent Cu compounds. The significant differences in the spectra indicate that Cu $4p$ states are important for the chemical bonding in these systems as was discussed above.

We particularly show that it is possible to, by means of Cu K$\beta_{2,5}$ XES, distinguish between the two monovalent Cu compounds Cu_2O and CuH that is especially useful in studies of copper corrosion in oxygen-free water. Figure 6.11 shows the Cu K$\beta_{2,5}$ spectra of Cu_2O and CuH. The intensity ratio between the two main features is different for Cu_2O and CuH and in agreement with predictions by local-density-approximation calculations. Furthermore the calculations predict the possible existence of three structures in the Cu K$\beta_{2,5}$ spectrum (for the experimental resolution used) of the Cu-O-H phase

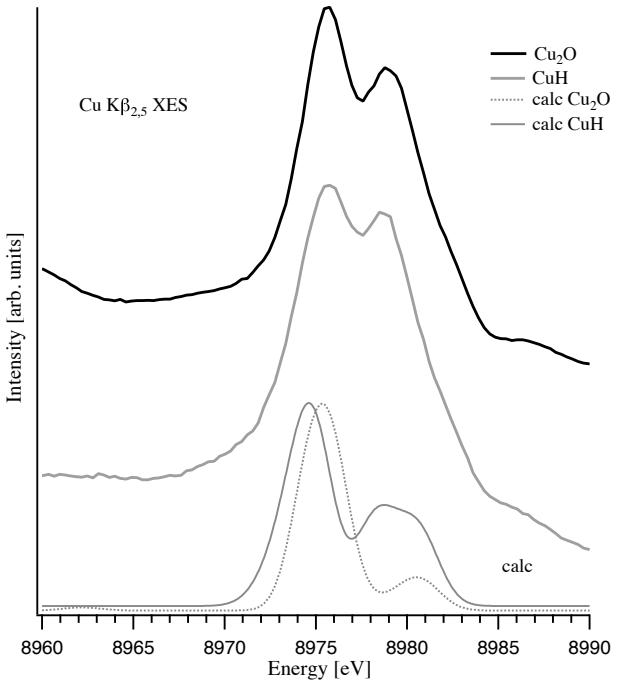

Figure 6.11: Cu K$\beta_{2,5}$ X-ray emission spectra of Cu_2O, CuH and Cu metal. On the bottom broadened Cu p DOSs of Cu_2O and CuH are shown.

of Cu(I) as a result of Cu 4s, p - O 2p - H 1s hybridization[29]. This makes it possible to detect the Cu-O-H phase formation if it is formed throughout the corrosion process in oxygen-free water.

As described in Paper VII we also showed that RIXS at the Cu K edge is a useful tool for studies of the electronic structure of monovalent Cu compounds since the experimental results can be reproduced by introducing the densities of states to the Kramers-Heisenberg equation as

$$F(\Omega,\omega) = \int_{\varepsilon} d\varepsilon \frac{\rho(\varepsilon)\rho'(\varepsilon+\Omega-\omega)}{(\varepsilon-\omega)^2+\frac{\Gamma^2}{4}} \tag{6.2}$$

where Ω and ω are incident and outgoing photon energies, ρ and ρ' are occupied and unoccupied densities of states and Γ is the lifetime broadening corresponding to the lifetime of the Cu 1s core-hole.

This makes RIXS a tool sensitive to differences in either or both occupied and unoccupied DOSs in different Cu compounds. Another potential advantage is that the experimental resolution in the RIXS process is not fundamentally limited by the lifetime broadening.

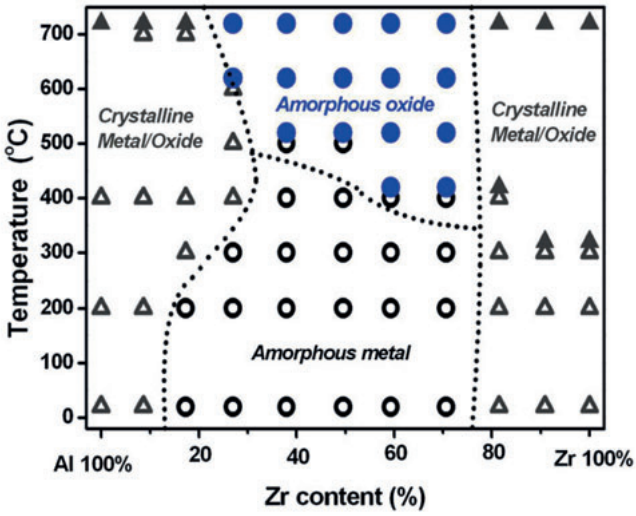

Figure 6.12: Phase diagram of Al-Zr systems.

6.4 Thermal treatment of amorphous alloys

6.4.1 Al-Zr

Amorphous Al-Zr alloys have been discussed as candidates for usage inside nuclear reactors. Both Al and Zr nuclei have low absorption cross-sections for thermal neutrons and they form amorphous structures for a large composition range. Amorphous structures prevent crack propagation and hydrogen and oxygen penetration through grain boundaries. Such properties are desirable for materials to be used inside nuclear reactors.

Extensive investigations of annealed Al_xZr_{100-x} alloys (and metals) are discussed in Paper VIII, leading up to a phase diagram as a final result. The phase diagram is shown in figure 6.12. The performed investigations include X-ray diffraction for structure determination, Rutherford backscattering spectrometry for composition confirmation, ellipsometry for determination of the thicknesses of the films and oxide layers, and photoelectron and X-ray spectroscopies for electronic structure investigations.

Figure 6.13 shows Al $L_{2,3}$ X-ray emission spectra of Al-Zr alloys (and metals) with different compositions. The spectral features are clearly different in terms of peak positions and relative intensities. When going from Al metal to compositions with higher Zr content the highest energy of observed occupied states decreases gradually. The energy of the maximum of the low-energy structure decreases with increasing Zr content while its relative weight increases. Al-Zr alloy with less than 17% Zr has previously been found in the crystalline phase or on the border between amorphous and crystalline phases. Hence, a phase transition is expected around the composition $Al_{80}Zr_{20}$. The

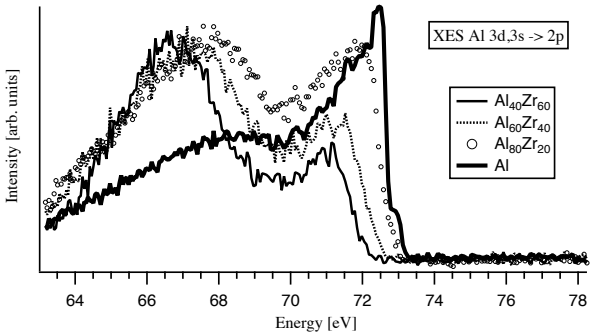

Figure 6.13: Al $L_{2,3}$ X-ray emission spectra of Al_xZr_{100-x}

difference between the spectral shapes of $Al_{40}Zr_{60}$ and $Al_{60}Zr_{40}$ is significantly smaller than that between $Al_{60}Zr_{40}$ and $Al_{80}Zr_{20}$ indicating a phase transition in between the two compositions from crystalline to amorphous structure.

Figure 6.14 shows O K X-ray absorption spectra of different Al-Zr compositions representing O 1*s* - 2*p* transitions of the oxide on the surface of the samples. The spectrum of the Zr sample resembles that of ZrO_2 in the tetragonal phase. With increasing Al content the spectral shape changes proportionally indicating that no phase transition occurs in the oxide layer with varying composition.

An interesting and poorly investigated question is how the electronic structure is changing when going from amorphous to crystalline structure and vice versa for the same composition. A brief look at the phase diagram in figure 6.12 reveals that it is possible to study how the electronic structure changes when going from amorphous to crystalline phase of for example $Al_{30}Zr_{70}$ without changing the composition, by annealing. This was investigated and presented in Paper IX.

Figure 6.15 shows Al $L_{2,3}$ X-ray absorption data of (a) the as-deposited Al film, (b) the as-deposited $Al_{73}Zr_{27}$ sample, (c) the $Al_{73}Zr_{27}$ film after annealing at 400°C and (d) the $Al_{73}Zr_{27}$ film after annealing at 700°C. The structures between 72 and 76 eV correspond to Al in the bulk Al-Zr and the structures above 76 eV correspond to oxidized Al in the form of Al_2O_3 The spectral shape in this range resembles that of γ-Al_2O_3 for all samples except for $Al_{73}Zr_{27}$ film after annealing at 700°C. Using these two regions we can study the electronic structure of both the oxide layer and the bulk alloy separately.

Considering the energy interval corresponding to the bulk alloy (72-76 eV) an interesting thing is worth to notice. The spectrum of the sample annealed at 400°C carries features of both the as-deposited (crystalline) Al film and the as-deposited (amorphous) $Al_{73}Zr_{27}$ sample. Those are a double-peak structure

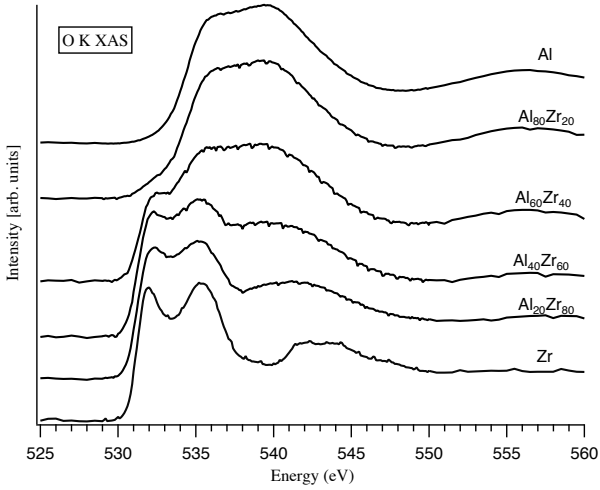

Figure 6.14: O K X-ray absorption spectra of Al_xZr_{100-x}

at ∼73 eV similar to that of as-deposited Al and a broad shoulder at ∼74-75 eV resembling that of as-deposited $Al_{73}Zr_{27}$. A combination of the two spectra is shown in figure 6.16. The particular combination (27% of crystalline Al and 73% of as-deposited $Al_{73}Zr_{27}$) corresponds to the best agreement with the spectrum of the sample annealed at 400°C, in terms of the spectral shape. We conclude that there are two phases in the annealed sample, namely amorphous Al-Zr and crystalline Al. The crystalline structure was visible in X-ray diffraction data which are only sensitive to the crystalline part.

Thus, this demonstrates that X-ray spectroscopy is sensitive to both amorphous and crystalline phases and, hence, complimentary to X-ray diffraction measurements.

The interpretation was supported by Al K X-ray absorption and Al $L_{2,3}$ X-ray emission measurements.

6.4.2 Fe-Zr

A combination of resistivity and X-ray spectroscopy measurements was performed on amorphous Fe-Zr alloys and multilayers. The most important finding was that resistivity data corresponding to different compositions were found to be remarkably different, while almost no differences were found in the spectroscopic measurements. The experiment is described in detail in Paper X.

These findings are illustrated in figures 6.17 and 6.18 representing the results of resistivity and X-ray spectroscopy measurements respectively. The X-ray absorption and emission spectra were recorded at the Fe $L_{2,3}$ edge. X-ray

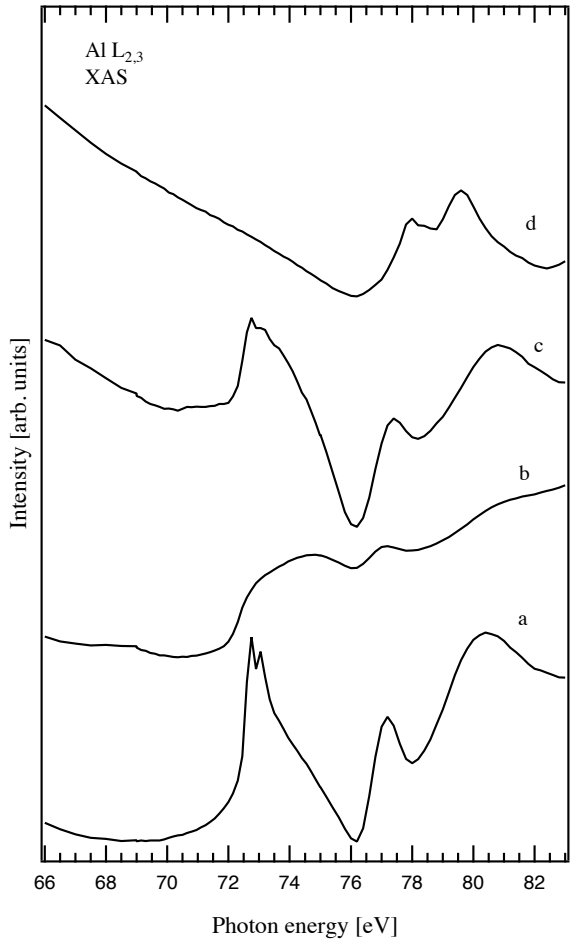

Figure 6.15: Al $L_{2,3}$ edge X-ray absorption spectra of four samples: (a) as-deposited Al film; (b) the as-deposited $Al_{73}Zr_{27}$ sample; (c) the $Al_{73}Zr_{27}$ film after annealing at 400°C; (d) the $Al_{73}Zr_{27}$ film after annealing at 700°C. The tilt of the background between 66 eV and 72 eV represents the contribution of the O 2*s* edge.

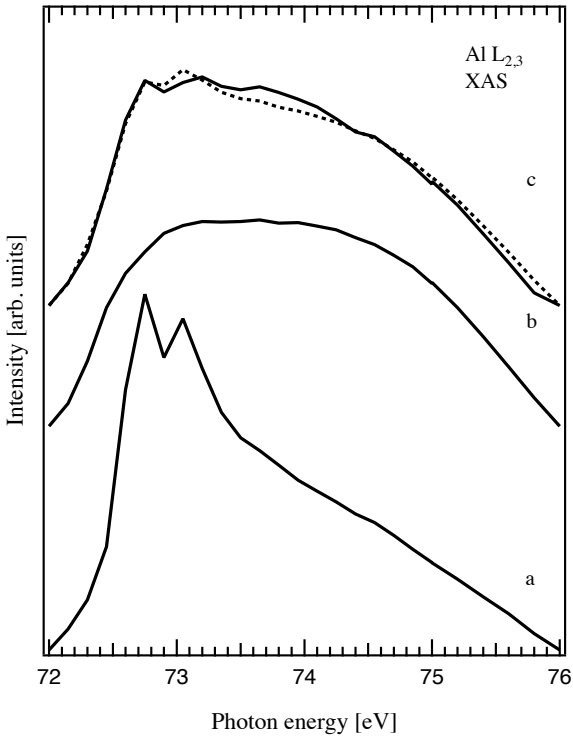

Figure 6.16: The 72-76 eV region of the Al $L_{2,3}$ XAS spectra of (a) as-deposited Al metal film, (b) as-deposited $Al_{73}Zr_{27}$ and (c) $Al_{73}Zr_{27}$ annealed at 400°C (all represented by solid lines) after subtraction of the linearly approximated background. The dashed curve is a simulated spectrum that represents a linear combination of spectra of crystalline Al (27% contribution) and as-deposited $Al_{73}Zr_{27}$ (73%) from this figure.

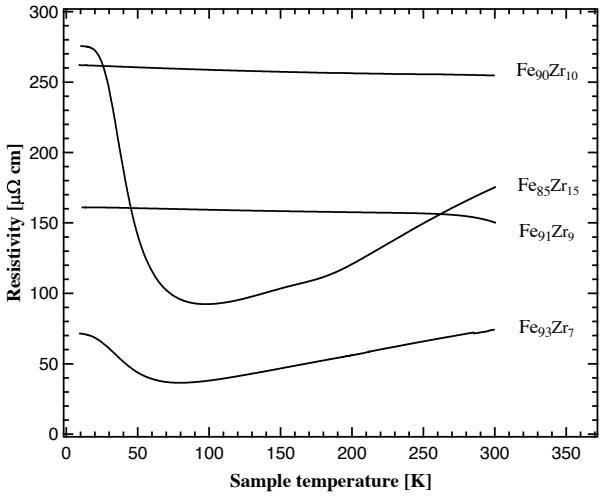

Figure 6.17: Resistivity measurements of Fe-Zr alloys with different compositions.

emission spectrum of $Fe_{93}Zr_7$ is represented by the solid (black) curve and the X-ray emission spectrum of $Fe_{85}Zr_{15}$ is displayed as the dashed (black) curve. All X-ray absorption spectra are shown as the red curve. The X-ray emission and absorption spectra represent, to some degree, the occupied and unoccupied densities of states respectively. The magnitude of the resistivity in the alloys is on the level of conductors. Conductors have no band gap between occupied and unoccupied density of states, hence, no band gap is expected in the studied alloys. The overlapping X-ray emission and absorption spectra confirm that there is no band gap.

However, the behavior of the resistivity data of two samples ($Fe_{93}Zr_7$ and $Fe_{85}Zr_{15}$) have regions of both decreasing and increasing resistivity. Increasing resistivity with temperature is typical for phonon scattering in metallic systems and decreasing resistivity is typical for semi-conductors. Semi-conductors are signified by a band-gap in the electronic structure. We interpret the decreasing resistivity as a sign of a localization effect due to the random structure of the amorphous alloy. Electrons can be trapped in regions in the potential landscape. The localization is associated with an activation energy which is reflected by the negative derivative of the temperature dependence of the resistivity in two samples.

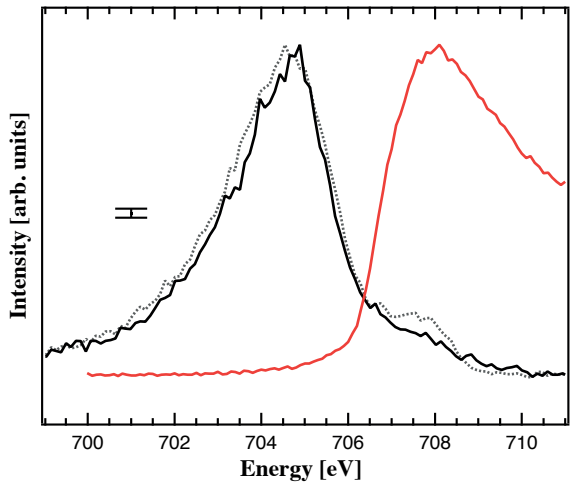

Figure 6.18: Fe $L_{2,3}$ edge X-ray emission (black) and absorption (red) spectra. Emission spectrum of $Fe_{93}Zr_7$ is represented by the solid (black) curve and the emission spectrum of $Fe_{85}Zr_{15}$ is represented by the dashed (black) curve. An X-ray absorption spectrum is represented by the red curve.

7. Acknowledgements

I would like to acknowledge Joseph Nordgren for letting me do my PhD in your group.

Many thanks to my supervisor Sergei Butorin for sharing your impressive knowledge in the field of X-ray spectroscopies!

Thank you Jan-Erik Rubensson for your encouraging attitude and for always taking time for simple PhD students despite a tight schedule. Thanks to everyone at the department, especially Stefan Plogmaker for providing chocolate in the darkest our.

Thank you Lars Werme for useful and interesting conversations about things that I know very little about, i.e., chemistry and exciting stories about the department from the seventies.

I would like to say thanks to Kristina Kvashnina, Inna Soroka and Björgvin Hjörvarsson for inspiring collaborations.

Thank you Johan Forsberg, Gunnar Pálsson and Fredric Ottermo for valuable input on the thesis.

I have certainly enjoyed sharing rooms and thoughts with Håkan Hollmark and Paw Kristiansen.

Thank you Filip Heijkenskjöld for redecorating my working space and for high-quality jokes at the right times.

I would like to thank my climbing and running friends who have provided necessary moments of distraction from research-related problems.

A huge thanks to my close friends and family who have always been very supporting and encouraging during the significant time of my life spent in the X-ray spectroscopy business!

Bibliography

[1] L. Werme. Design premises for canister for spent nuclear fuel. Technical report, September (1998).

[2] G. Hultquist. *Corrosion Science*, **26**:173, (1986).

[3] G.Hultquist, M. J. Graham, P. Szakalos, G. I. Sproule, A. Rosengren, and L. Gråsjö. *Corrosion Science*, **53**:310, (2011).

[4] H. W. Sheng, W. K. Luo, F. M. Alamgir, J. M. Bai, and E. Ma. *Nature*, **439**:419, (2006).

[5] K. H. J Buschow and P. H. Smit. *Journal of Magnetism and Magnetic Materials*, **23**:85, (1981).

[6] S. Ohnuma, K. Shirakawa, M. Nosea, and T. Masumoto. *IEEE Transactions on Magnetics*, **16**:1129, (1980).

[7] Z. S. Wronski, A. H. Morrish, and A. M. Stewart. *Physics letters*, **101**:294, (1984).

[8] S. M. Fries, H-G. Wagner, S. J. Campbell, U. Gonser, N. Blaes, and P. Steiner. *Journal of Physics F: Metal Physics*, **15**:1179, (1985).

[9] C. Arakawa M. Itakura, H. Kaburak. *Physical Review E*, **71**:1, (2005).

[10] I. L. Soroka, J. Vegelius, P. T. Korelis, A. Fallberg, S. M. Butorin, and B. Hjörvarsson. *Journal of Nuclear Materials*, **401**:38, (2010).

[11] J. J. Sakurai. *Advanced Quantum Mechanics*. Addison-Wesley, (1967).

[12] C. Nordling and J. Österman. *Physics Handbook for Science and Engineering*. Carl Nordling, Johnny Österman and Studentlitteratur, 8th edition, (2006).

[13] B. H. Bransden and C. J. Joachain. *Physics of Atoms and Molecules*. Pearson Education Limited, 2nd edition, (2003).

[14] D. W. Snoke. *Solid State Physics, Essential concepts*. Addison-Wesley, (2009).

[15] E. Z. Kurmaev, J. van Ek, D. L. Ederer, L. Zhou, T. A. Callcott, R. C. C. Perera, V. M. Cherkashenko, S. N. Shamin, V. A. Trofimova, S. Bartkowski, M. Neumann, A. Fujimori, and V. P. Moloshag. *Journal of Physics, Condensed Matter*, **10**:1687, (1998).

[16] J.-E. Rubensson. *Journal of Electron Spectroscopy and Related Phenomena*, **110**:135, (2000).

[17] F. M. F. de Groot. *Physical Review B*, **53**:7099, (1996).

[18] J. Nordgren and J. Guo. *Journal of Electron Spectroscopy and Related Phenomena*, **110**:1, 2000.

[19] J. Nordgren and R. Nyholm. *Nuclear Instruments and Methods in Physics Research*, **246**:242, (1986).

[20] P. Glatzel and U. Gergmann. *Coordination Chemistry Reviews*, **249**:65, (2005).

[21] J. M. Haschke, T. H. Allen, and L. A. Morales. *Science*, **287**:285, (2000).

[22] S. M. Butorin, K. O. Kvashnina, A. Modin, J.-H. Guo, D. K. Shuh, L. Werme, and J. Nordgren. Tr-09-08. Technical report, (2009).

[23] I. Nakai, Y. Sugitani, K. Nagashima, and Y. Niwa. *J. Inorg. Nucl. Chem.*, **40**:789, (1978).

[24] J. C. W. Folmer and F. Jellinek. *Journal of the Less-Common Metals*, **76**:153, (1980).

[25] H. T. Evans and J. A. Konnert. *American Mineralogist*, **61**:996, (1976).

[26] S. W. Goh, A. N. Buckley, and R. N. Lamb. *Minerals Engineering*, **19**:204, (2006).

[27] J. P. Simpson and R. Schenk. *Corrosion Science*, **27**:1365, (1987).

[28] T. E. Eriksen, P. Ndalamba, and I. Grenthe. *Corrosion Science*, **29**:1241, (1989).

[29] P A Korzhavyi and B Johansson. Thermodynamic properties of copper compounds with oxygen and hydrogen from first principles. Technical report, February (2010).

Acta Universitatis Upsaliensis

Digital Comprehensive Summaries of Uppsala Dissertations from the Faculty of Science and Technology 874

Editor: The Dean of the Faculty of Science and Technology

A doctoral dissertation from the Faculty of Science and Technology, Uppsala University, is usually a summary of a number of papers. A few copies of the complete dissertation are kept at major Swedish research libraries, while the summary alone is distributed internationally through the series Digital Comprehensive Summaries of Uppsala Dissertations from the Faculty of Science and Technology.

Distribution: publications.uu.se
urn:nbn:se:uu:diva-160362

ACTA
UNIVERSITATIS
UPSALIENSIS
UPPSALA
2011